Ionospheric Effects on Network-RTK

Ragne Emardson, Per Jarlemark, Jan Johansson, and Sten Bergstrand

SP Technical Research Institute of Sweden

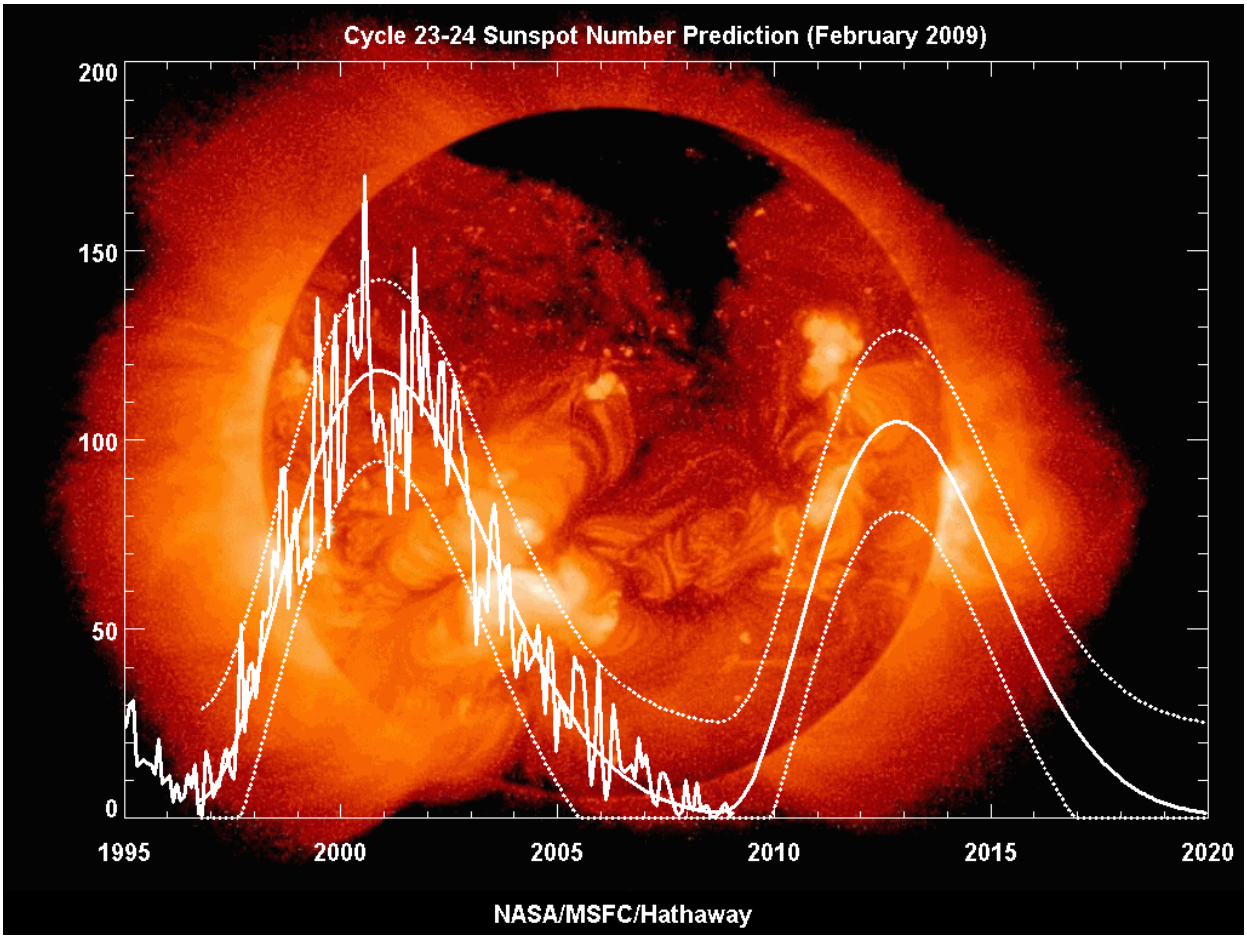

Credit: David Hathaway, NASA/MSFC, http://science.nasa.gov/science-news/science-at-nasa/2009/01apr_deepsolarminimum/.

Measurement Technology

SP Report 2011:80

Ionospheric Effects on Network-RTK

Ragne Emardson, Per Jarlemark, Jan Johansson, and Sten Bergstrand

Abstract

Ionospheric Effects on Network-RTK

A part of the atmosphere is ionized by the UV radiation from the Sun. This part is often referred to as the ionosphere. The resulting free electrons influence the GNSS signals as they propagate through the ionosphere. We have studied how the spatial variations of electron density in the ionosphere affect measurements with network-RTK. The aim is to predict what we can expect from measurements during the next solar maximum that is expected to occur around 2012. In order to perform a spatial characterization of the ionosphere, we have used archived GPS data from SWEPOS from a five year period, 1999-2004, around the previous solar maximum.

We find that the effect of the ionospheric spatial variability on network-RTK measurements is greater during night time than during day time. It is also clear that the effect is larger for northern Sweden than for the southern part. This is especially true during night time. The effect is also largest in the months October and November and smallest in June and July. Also the number of cycle slips is larger in northern Sweden than in southern Sweden. We find that when monitoring the ionosphere and its influence on network-RTK performance it is desirable to have several different geographical regions under observation. The effects in northern Sweden may, for example not be that relevant for a user in southern Sweden.

In this report we define the ionospheric delay errors as the standard deviation of the difference between the ionospheric delay at L1 at one location and the estimated value of this based on the three surrounding reference stations with 70 km separation. Using GNSS equipment that is state-of-the art around 2010, we find that when conditions are such that the ionospheric delay error is below 10 mm, which occurs some 70% of the time, a rover is able to fix the ambiguities more than 90% of the time. This ability decreases with increasing ionospheric variability and when the ionospheric delay error is larger than 25 mm, which occurs some 10% of the time, the rover ability to fix is less than 50%. When measuring with network-RTK during the next solar maximum, approximately, 80% of the time, we have conditions such that a rover has at least 75% chance of fixing the solutions.

Overall the probability to find a correct fix solution when performing RTK measurements during the next solar maximum is approximately 85% and the mean time to fix is 55 seconds.

Key words: Ionosphere, GPS, RTK, uncertainty

SP Sveriges Tekniska Forskningsinstitut
SP Technical Research Institute of Sweden

SP Report 2011:80
ISBN 978-91-87017-13-1
ISSN 0284-5172
Borås

Contents

Preface

This report is a result of the project Close II which is a collaboration between SP, Chalmers University of Technology and Lantmäteriet. The purpose of the project is to predict what we can expect from measurements with network-RTK during the next solar maximum that is expected to occur around 2012.

Sammanfattning

En del av atmosfären joniseras av UV-strålning från solen. Denna del är ofta kallad jonosfären. De fria elektronerna som bildas påverkar GNSS signalerna som propagerar genom jonosfären. Vi har studerat hur den rumsliga variationen av elektrontätheten i jonosfären påverkar mätningar med nätverks-RTK. Syftet är att förutsäga vad vi kan förvänta oss av mätningar under nästa solmaximum som väntas inträffa runt 2012. För att karakterisera jonosfären har vi använt arkiverade GPS-data från SWEPOS från en femårs period runt föregående solmaximum.

Vi finner att effekten av jonosfärens rumsliga variationer på mätningar med nätverks-RTK är större nattetid än dagtid. Det är också tydligt att effekten är större för norra Sverige än för den södra delen. Detta gäller särskilt nattetid. Effekten är också störst under månaderna oktober och november och minst i juni och juli. Också antalet ”cycle slips” är större i norra Sverige än i södra Sverige. Vi finner att vid övervakningen av jonosfären och dess påverkan på prestanda vid mätningar med nätverks-RTK är det önskvärt att observera flera olika geografiska regioner. Effekterna i norra Sverige är till exempel inte nödvändigtvis relevanta för en användare i södra Sverige.

I denna rapport definierar vi jonosfärens rumsliga variationer som standardavvikelsen av skillnaden mellan en punkts jonosfärsfördröjning på L1 och det uppskattade värdet av denna baserat på tre omgivande referensstationer med 70 km separation. Med dagens utrustning, finner vi att när förhållandena är sådana att de rumsliga variationerna i jonosfären är lägre än 10 mm, vilket sker ungefär 70% av tiden, klarar en rover av att kunna mäta korrekt mer än 90% av tiden. Denna förmåga minskar med en ökande jonosfärsvariabilitet och när denna är större än 25 mm, vilket sker cirka 10% av tiden, är förmåga att mäta korrekt mindre än 50%. Vid mätning med nätverks-RTK under nästa solmaximum, kommer vi att cirka 80% av tiden ha sådana villkor att en rover har minst 75% chans att fungera korrekt.

Totalt är sannolikheten för att kunna hitta en korrekt lösning vid mätningar med nätverks-RTK under nästa solmaximum cirka 85% och den genomsnittliga tiden för en rover att finna denna lösning är 55 sekunder.

1 Introduction

A part of the atmosphere is ionized by the UV radiation from the Sun. This part is often referred to as the ionosphere. The resulting free electrons influence the GNSS signals as they propagate through the ionosphere. The phase of the signal is advanced by an amount of time, δt, while the pseudorandom code is delayed by the same amount.

$$\delta t = \frac{40.3}{c_0 f^2} \int_S N_e ds \tag{1}$$

where c_0 is the speed of light in vacuum, f is the signal frequency, N_e is the total number of free electrons along the signal path S. Frequency dependent delay terms of higher order exist. The dominant part is a third order effect originating from the earth magnetic field.[*Kedar et al.*, 2003] This effect is relatively small and the magnetic field can be considered constant over the spatial scales relevant for network-RTK. Hence, the size of this effect is negligible in this study. The quantity

$$\int_S N_e ds \tag{2}$$

is usually referred to as the total electron content (TEC). As seen from (1), the size of the effect depends on the signal frequency. Using GNSS data that is transmitted on two frequencies, it is thus possible to form a new observable that, to the first order, is insensitive to the effect of the ionosphere. Using the L1 and L2 observables from GPS this combination can be written as [e.g., *Hoffman-Wellenhof et al.*, 1994].

$$L_3 \approx 2.55 L_1 - 1.55 L_2 \tag{3}$$

Emardson et al. [2009] show that the contribution from the ionosphere can be one of the dominating error sources in network-RTK. When using the L1 observable only for determining a position this contribution will under different circumstances be the single largest error contribution. Using the ionosphere free L3 observable this effect is removed, although, at the expense of the contribution from the contribution from the local effects [*Emardson et al.*, 2009].

From GPS we can also form the combination

$$L_4 = L_1 - L_2 \tag{4}$$

This combination removes all frequency independent effects such as geometry, signal delay in the troposphere, satellite and receiver clocks etc. A fraction of the ionospheric effect on the two frequencies is however left. Hence this combination can be used to derive information about the ionosphere.

The activity of the Sun is observed in cycles of eleven years duration. At the time of the writing of this report, we are in a minimum of activity. The next solar maximum is expected to be around 2012. In this report we have studied the effect of ionospheric variations on the results from measurements using network-RTK.

2 Characterization

2.1 Solar activity

The sun emits electromagnetic energy with a slowly varying intensity. This flux changes gradually from day-to-day. The activity of the sun is associated with the sunspot cycle, with more radiation occurring at radio frequencies as well as in the UV-region with more sunspots. The amount of received radiation also varies with geographical location.

The amount of ionization in the ionosphere is correlated with the amount of radiation received from the sun. The ionosphere is often divided in several layers or regions which are shown in Figure 1. These are named D, E, and F regions starting as seen from the Earth. The D region extends from around 50 km above the surface of the Earth to 90 km. The E region is between 90 km and 120 km while the F region, situated at 120 km to 400 km above the surface of the Earth, is the top most layer of the ionosphere and is also the part of the ionosphere that has the greatest effect on the GNSS signals. Here the solar radiation ionizes the atomic oxygen. The F layer consists of one layer at night, but in the presence of sunlight i.e., during daytime, it divides into two layers, usually referred to as F_1 and F_2.

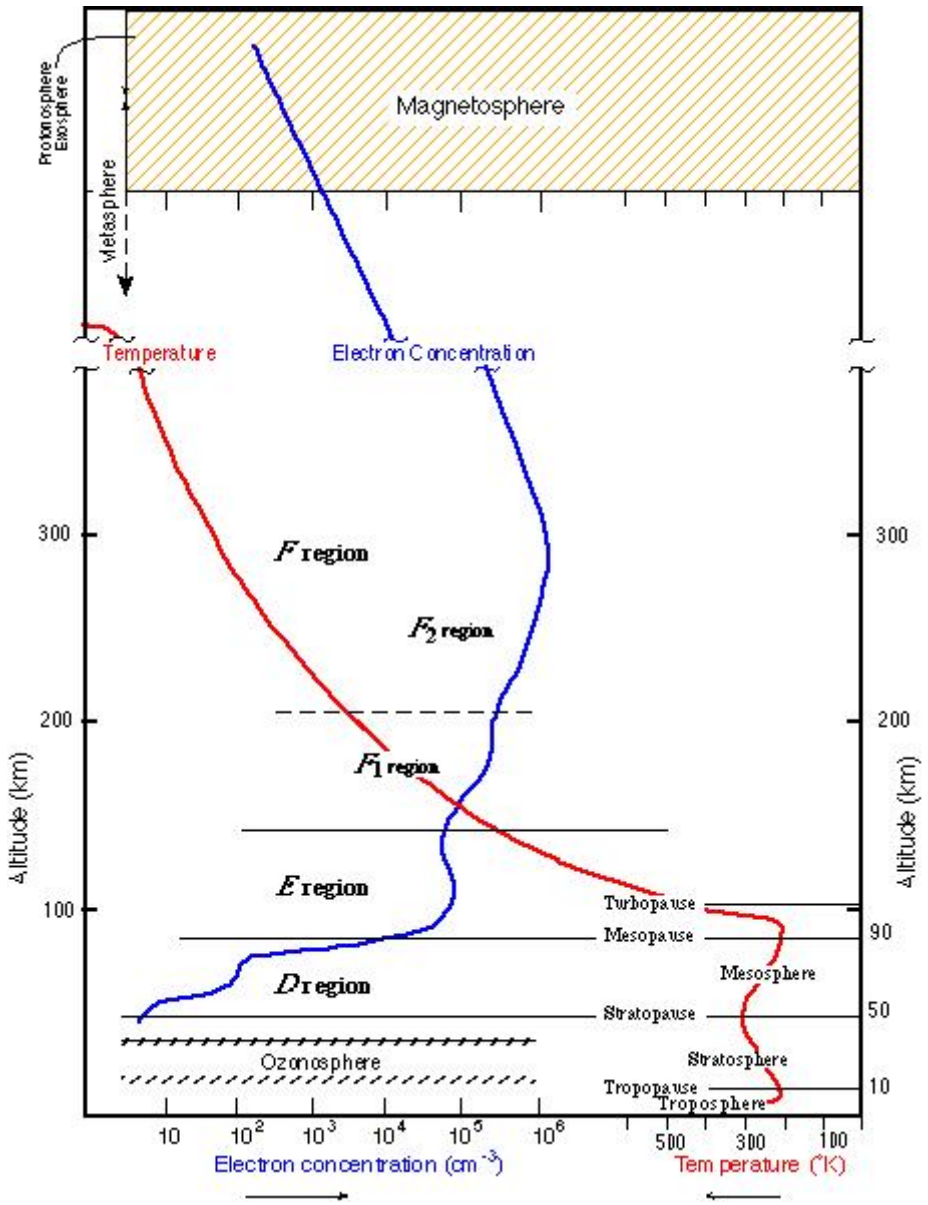

Figure 1 **Electron distribution as a function of height above the Earth's surface (From http://ion.le.ac.uk/ionosphere/profile.html)**

There are also other mechanisms that disturb the ionosphere. One example is solar flares. When the sun is active, strong solar flares can occur. These are large explosions in the Sun's atmosphere that release large amount of energy. The radiation hit the Earth with X-rays which penetrate all the way down to the D-region and release electrons. The solar flares also release charged particles into the solar wind which reaches the Earth and interacts with its geomagnetic field. Most flares occur in regions around sunspots. Solar flares accelerates electrons, protons, and heavier ions to near the speed of light. They produce radiation across the electromagnetic spectrum at all wavelengths, from radio waves to gamma rays.

The solar cycle has traditionally been observed by counting the frequency and placement of sunspots visible on the Sun. A sunspot is an area on the Sun's surface that is marked by intense magnetic activity, forming areas of reduced surface temperature. They can be visible from Earth without the aid of a telescope. Figure 2 shows the annual number of sunspots during almost 300 years.

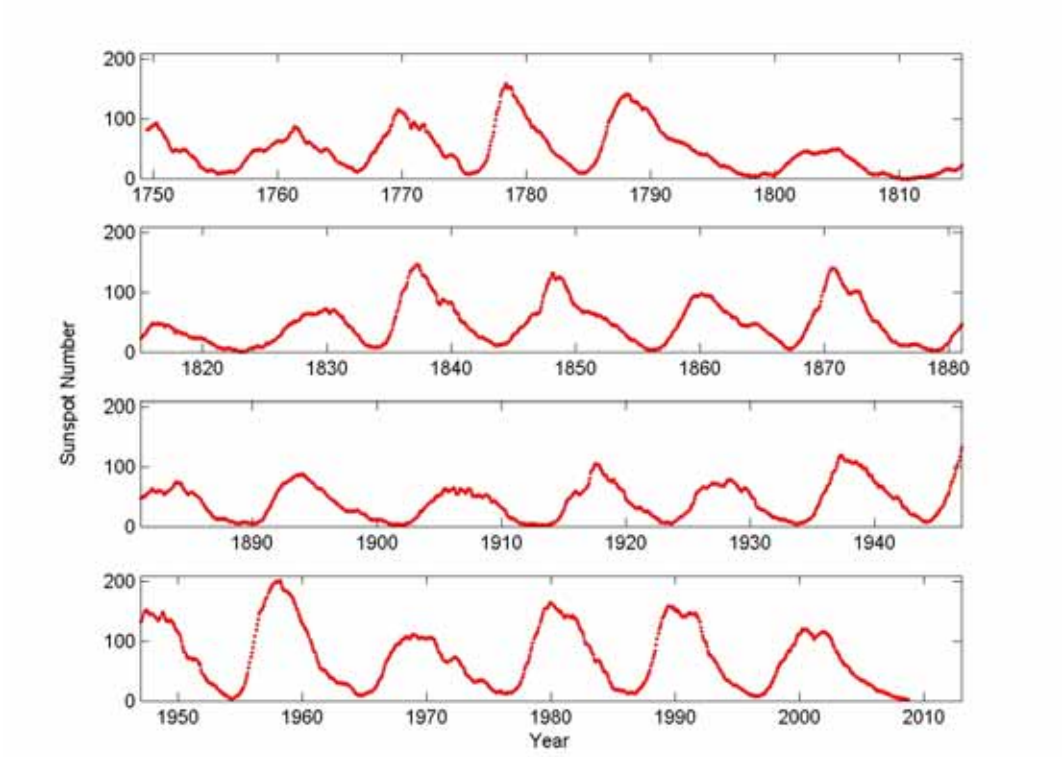

Figure 2 Number of observed Sunspots.

Another measure of the solar activity is the F10.7 index. It is a measure of the noise level generated by the sun at a wavelength of 10.7 cm as observed at the earth's orbit. Figure 3 shows the number of observed sunspots together with the measured solar flux at 10.7 cm starting in the 1940's until today. We can see that there is a clear correlation between the number of sunspots and the received solar flux.

Table 1 includes a summary of the different physical phenomena.

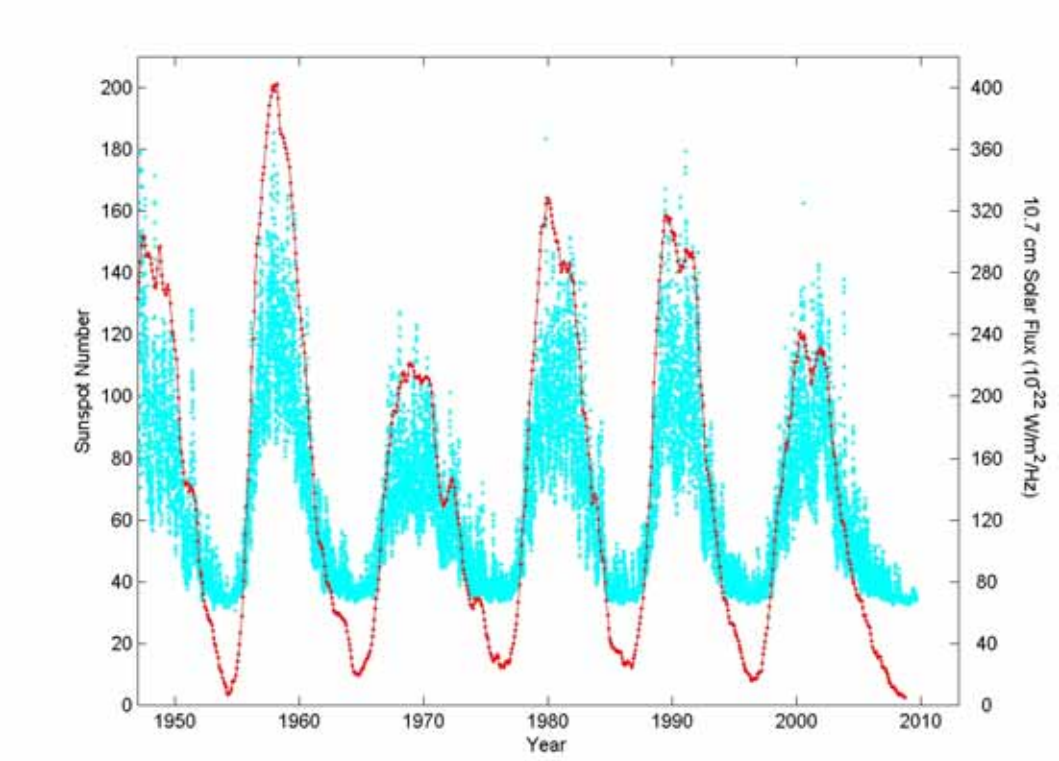

Figure 3 **Number of observed Sunspots (red) and measured solar flux at 10.7 cm (blue).**

Table 1 Terminology

Term	Explanation
Solar flare	A solar flare is a large explosion in the Sun's atmosphere that can release much energy. It accelerates electrons, protons, and heavier ions to near the speed of light and emits radiation at all wavelengths. Most flares occur in active regions around sunspots
Solar wind	The solar wind is a plasma, composed primarily of electrons and lone protons
Geomagnetic storm	Disturbances in the geomagnetic field caused by gusts in the solar wind that blows by Earth.
Solar radiation storm	Elevated levels of radiation that occur when the numbers of energetic particles increase.
Radio blackout	When solar flares hit the Earth with hard X-rays on the sunlit side of the Earth that penetrate to the D-region and results in radio blackout
Sunspots	A sunspot is an area on the Sun's surface that is marked by intense magnetic activity
Solar radiation	See solar flux
Solar flux	The sun emits radio energy with a slowly varying intensity. This quantity is often measured e.g, at the wavelength 10.7 cm
TEC	Total Electron Content. The Integrated amount of free electrons along the signal path usually in el/m^2 or TECU. 1 TECU equals 10^{16} el/m^2.
Travelling Ionospheric Disturbance (TID)	A wave in the electron density structure that propagates horizontally which affects the refraction of radio waves. TIDs are often divided in large-scale, medium-scale and small-scale.

2.2 The Ionosphere and GNSS

Figure 4 shows the number of observed sunspots, measured solar flux at 10.7 cm and vertical TEC over Sweden estimated from GPS data. The data covers the period 1995 to 2009, which includes the previous solar maximum. The vertical bars indicate the time period 1999 to 2004 that we study in more detail in this report. Hereafter, we refer to this period as the focus period. From the figure it is clear that the amount of free electrons are correlated with the both the solar flux and the number of sunspots. This can be interesting to note as the physical process behind the generating of free electrons is based on radiation at wavelengths around the UV, which is very far from the 10.7 cm wavelength used for the solar flux measurements.

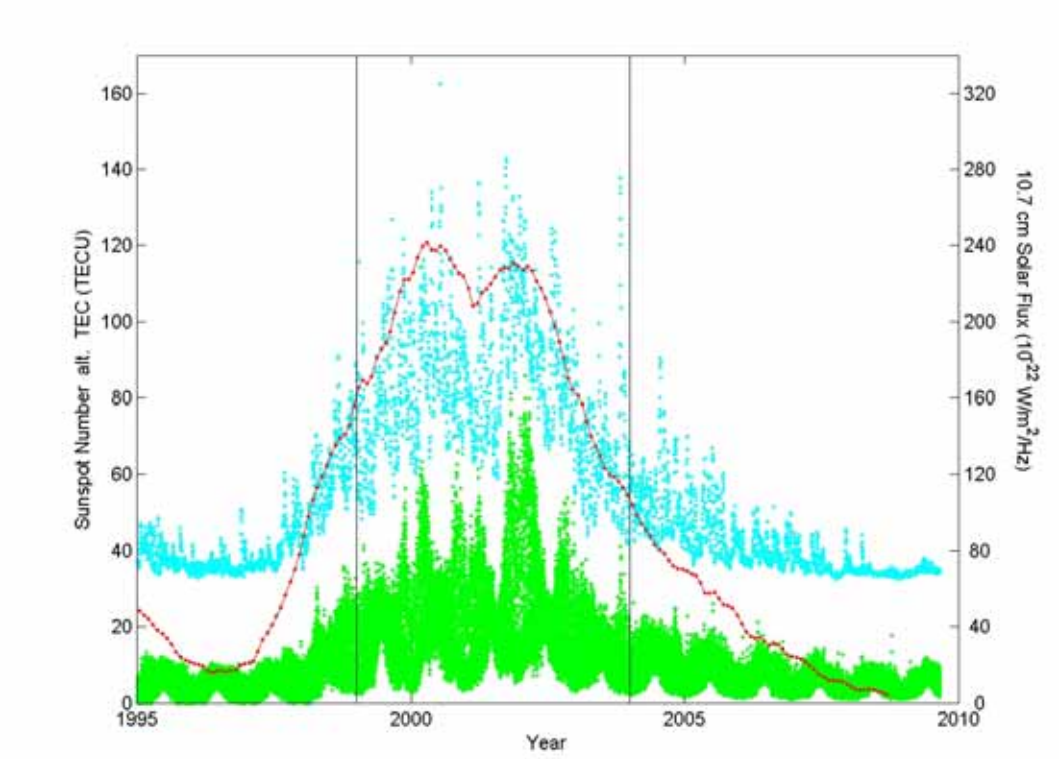

Figure 4 **Number of observed Sunspots (red), measured solar flux at 10.7 cm (blue) and vertical TEC over Sweden estimated from GPS data (green).**

Figure 5 shows the vertical TEC over Sweden for the focus period used in this study estimated from GPS data. The red line is a least squares fit of a second-degree polynomial to the TEC data. According to these data, the solar maximum occurred during 2001.

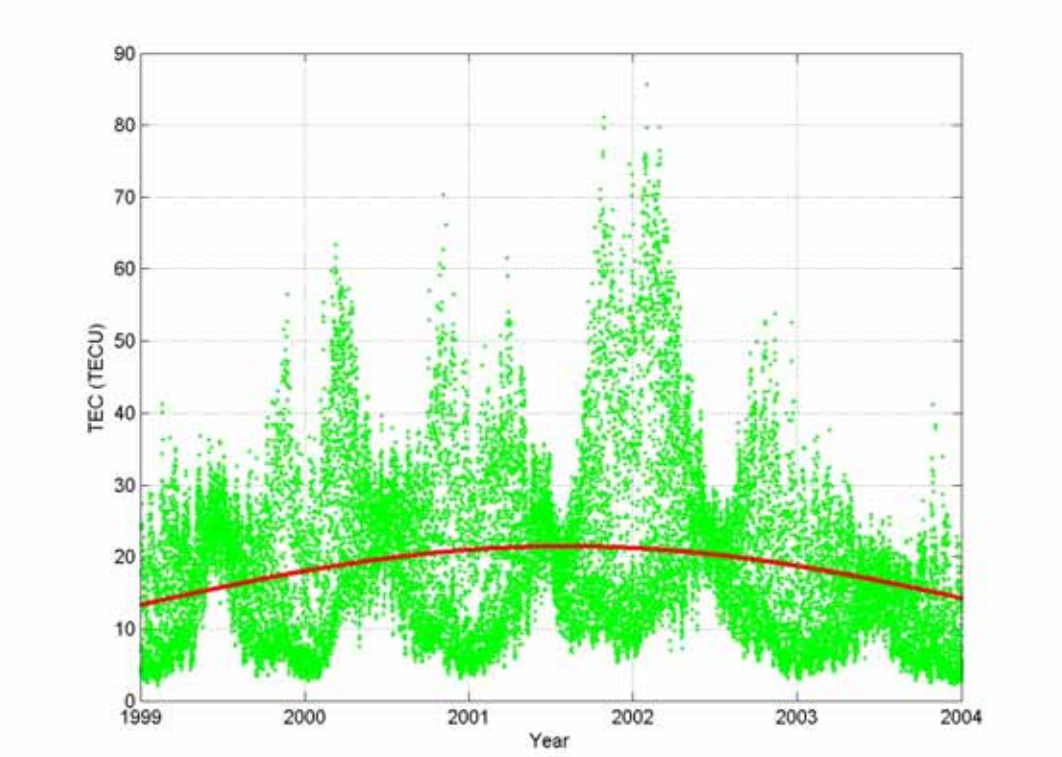

Figure 5 **Vertical TEC over Sweden estimated from GPS data. The red line is a least squares fit of a second-degree polynomial to the TEC data.**

2.3 Spatial Characterization

We have studied the spatial variations of the ionospheric variations on scales relevant for network-RTK using data from the previous solar maximum. The aim is to predict what we can expect during the next solar maximum. In order to perform a spatial characterization of the ionosphere, we used archived GPS data from SWEPOS. We imitated the structure in network-RTK by using data from stations forming geographical triangles with approximately 250 km between the reference stations. Figure 6 shows the geographical locations of the sites we use in this study. The characterization is performed by using observations of the ionospheric delay from the three sites forming a triangle in order to interpolate the expected ionospheric delay for the site in the middle of the triangle. We then compare the interpolated time series with those actually measured. The difference between these two timeseries can be considered as the interpolation error. We obtain interpolation errors for the three triangles. Hereafter we refer to the upper or northern triangle as North Triangle, the mid triangle as Mid Triangle, and the southern triangle as South Triangle. In this study, North Triangle consists of the sites Arjeplog, Umeå, and Oulu (Finnref) interpolating the site Skellefteå, Mid Triangle consist of Karlstad, Mårtsbo, and Sveg interpolating the site Leksand, and South Triangle consist of Vänersborg, Hässleholm, and Norrköping interpolating the site Jönköping. The data for the South and Mid triangles were provided at a 15 s rate, while the data for the North triangle were provided at a 30 s rate.

For each site in a triangle we form the L4 (L1-L2) combination for a specific satellite observation. We use the L4 combination from the three surrounding sites in the triangle to interpolate an expected L4 at the inner site. The interpolation is performed through bilinear interpolation in latitude and longitude. This is essentially the same as fitting a plane surface to the values of the surrounding triangle and use that information to determine the value of the inner site. We use only cycle slip free satellite passes that are

longer than 1 hour and with the satellite observation above 20^o in elevation. The passes we use is typically a couple of hours. We compute the difference between the interpolated and measured L4 values. From this difference we subtract its mean value, assuming it mainly originates from the ambiguous phase constants. These resulting differences are then mapped to zenith in order to be comparable with each other. We use the mapping function

$$m_i(\varepsilon) = \frac{1}{\cos\left(\arcsin\left(\frac{R\sin(\varepsilon + \pi/2)}{R+h}\right)\right)} \tag{5}$$

where ε is the elevation angle of the observation, *R* is the radius of the earth and *h* is the height of the ionosphere, here at 400 km, represented as a thin shell.

This procedure is performed for all observed satellites. We use these computed differences from all observed satellites to form hourly root mean square (rms) values. For these calculations we have used the L4 combination. For simplicity, we prefer to express the results on the L1 frequency. Hence we convert the results to correspond to ionospheric delay variability for signals on the L1 frequency. We then remove the expected contribution from multipath, 3.8 mm, [*Emardson et al.*, 2009] from our computed rms values to obtain the sought information about the ionospheric variability. See Appendix I for more details on the rationales for the spatial characterization of the ionosphere.

Figure 7, Figure 8, and Figure 9 show the resulting rms differences between the interpolated and measured ionosphere for North Triangle, Mid Triangle, and South Triangle respectively. The results are shown for the entire focus period. There seems to be periodic variations with larger errors during winter time.

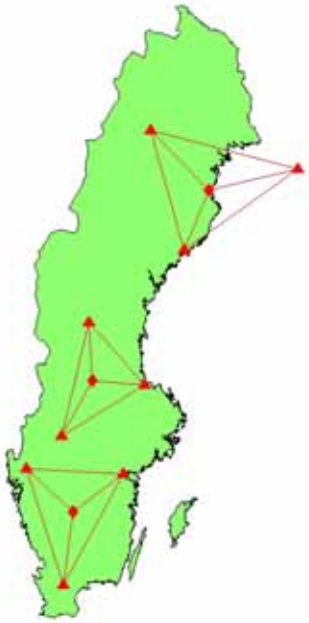

Figure 6 **Map of Sweden showing the three triangles used for investigating the ionosphere interpolation error.**

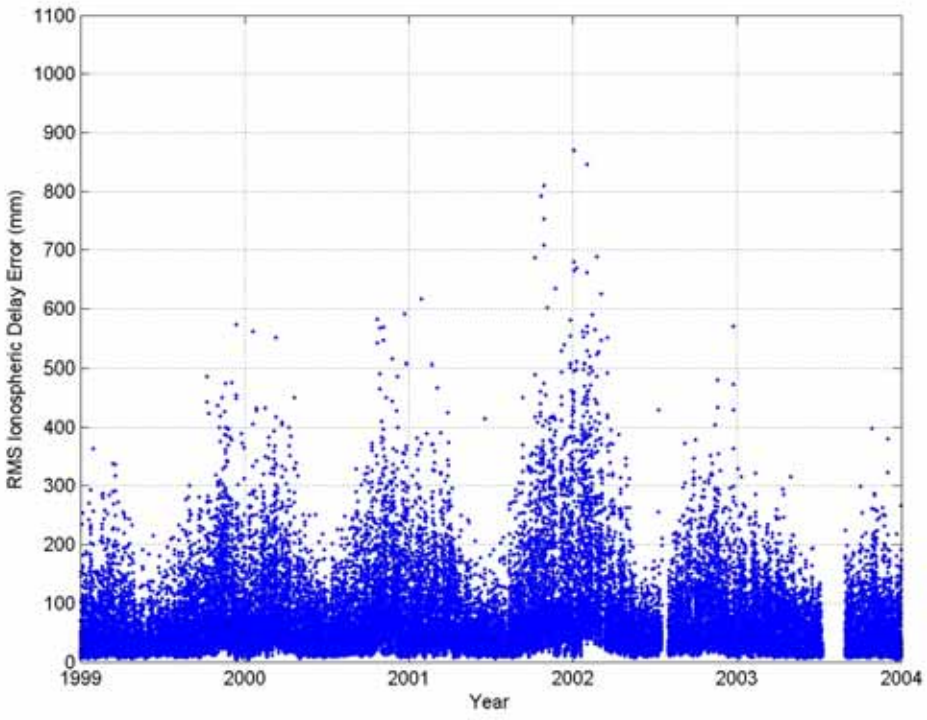

Figure 7 **L1 ionospheric interpolation error over North Triangle. Values are hourly errors.**

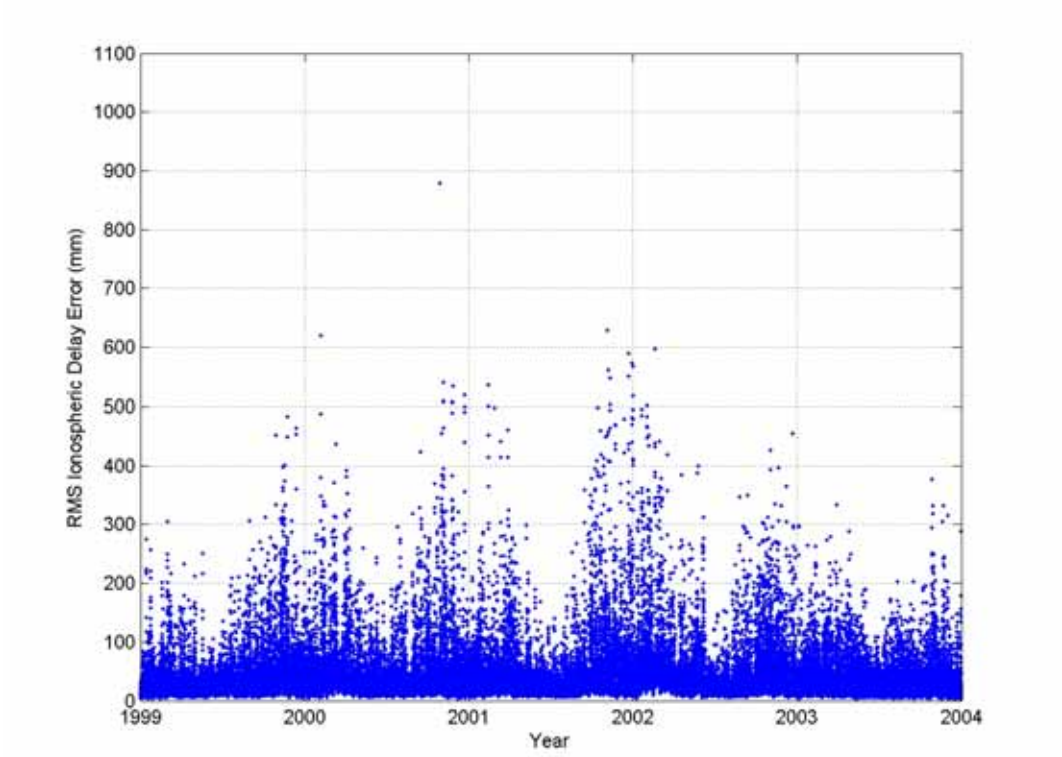

Figure 8 **L1 ionospheric interpolation error over Mid Triangle. Values are hourly errors.**

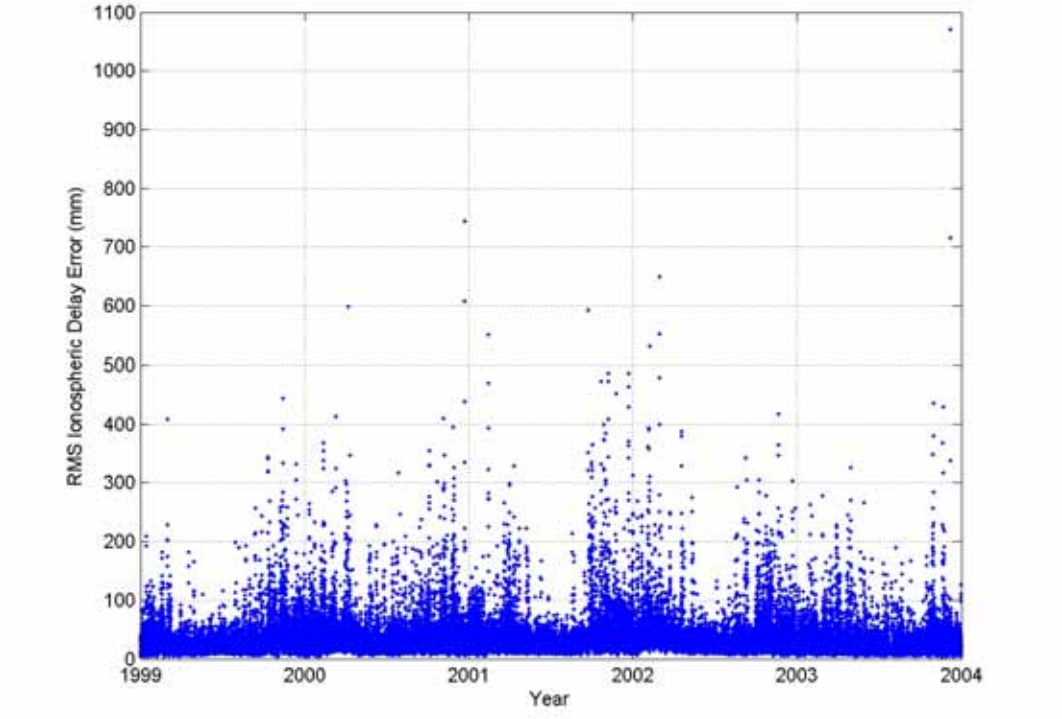

Figure 9 **L1 ionospheric interpolation error over South Triangle. Values are hourly errors.**

The distance between the reference stations in the triangles in Figure 6 are larger than those we assume for a standard reference network, i.e., with 70 km between the reference sites. In order to use the results for such networks, we have scaled the results using a distance scale factor. We have used a scaling that is linear with distance, [*Emardson et al*., 2010]. This scaling is based on studies where we use different sizes of triangles for interpolation. Figure 10, Figure 11, and Figure 12 show the hourly rms differences between the interpolated ionosphere and the measured ionosphere for North Triangle Mid Triangle and South Triangle respectively scaled to correspond to networks with 70 km between the reference stations. In this report we will hereafter always use these scaled results.

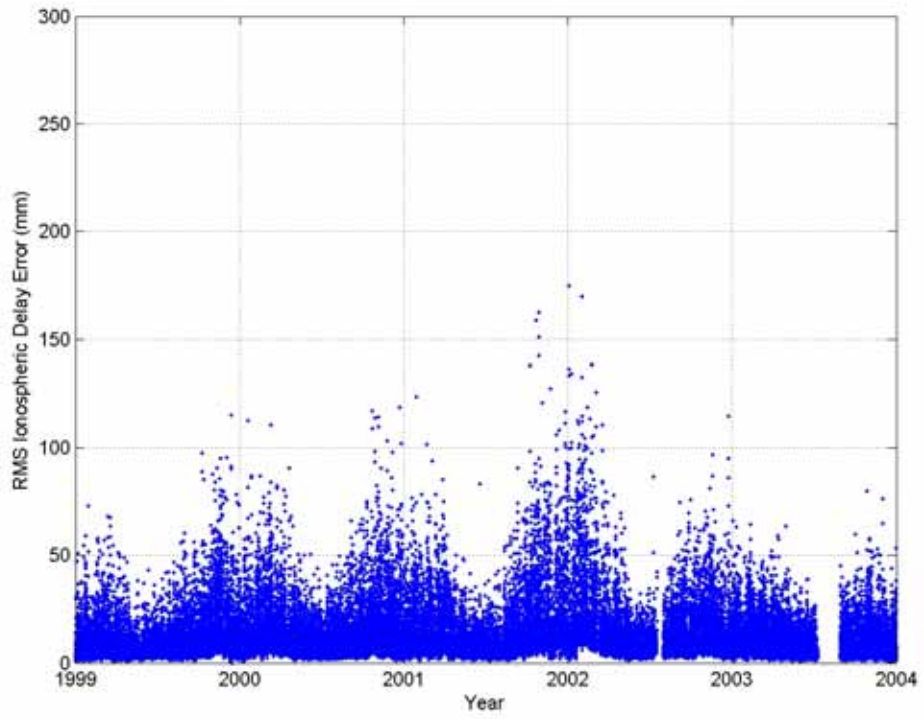

Figure 10 **L1 ionospheric interpolation error over North Triangle. Values are hourly errors. Values have been scaled to represent a network of nominal size of 70 km between the reference stations.**

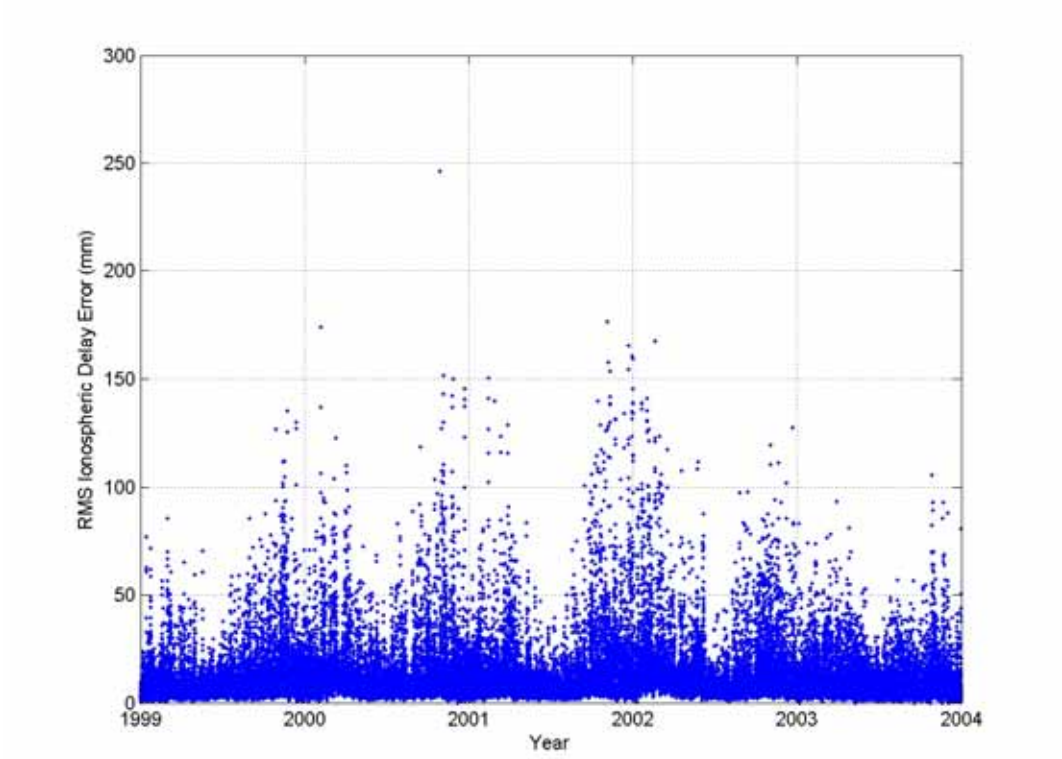

Figure 11 **L1 ionospheric interpolation error over Mid Triangle. Values are hourly errors. Values have been scaled to represent a network of nominal size of 70 km between the reference stations.**

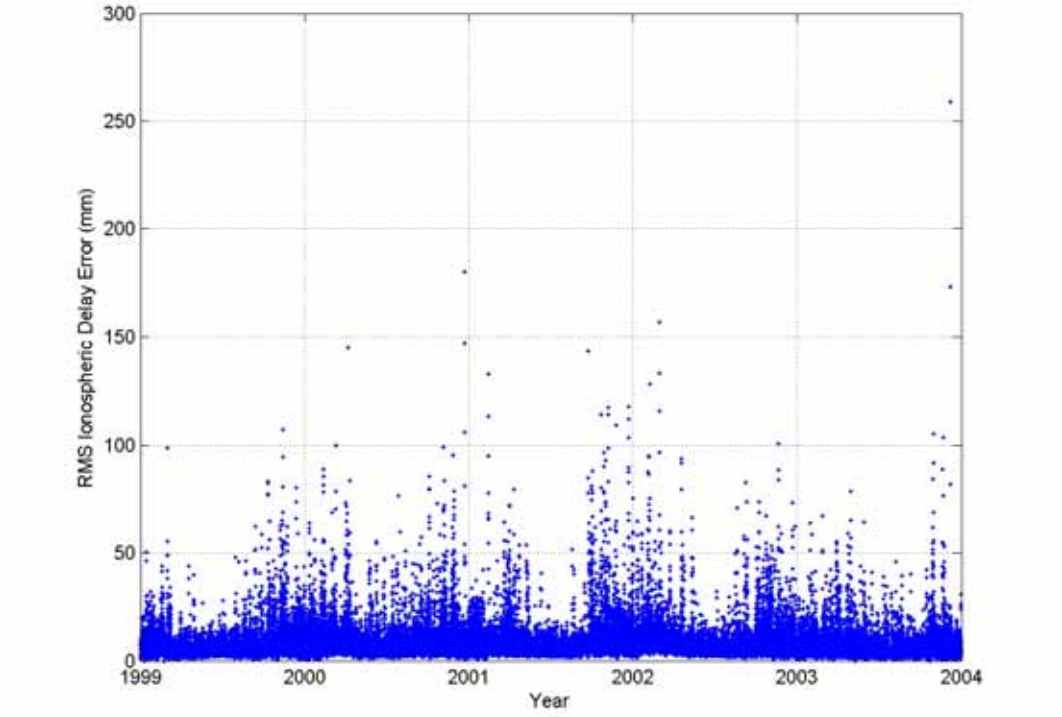

Figure 12 **L1 ionospheric interpolation error over South Triangle. Values are hourly errors. Values have been scaled to represent a network of nominal size of 70 km between the reference stations.**

Figure 13, Figure 14, and Figure 15 show the histogram over the ionospheric interpolation error over North Triangle, Mid Triangle, and South Triangle. These distributions will be the input to the different processes that we use to study network-RTK performance under different ionospheric conditions.

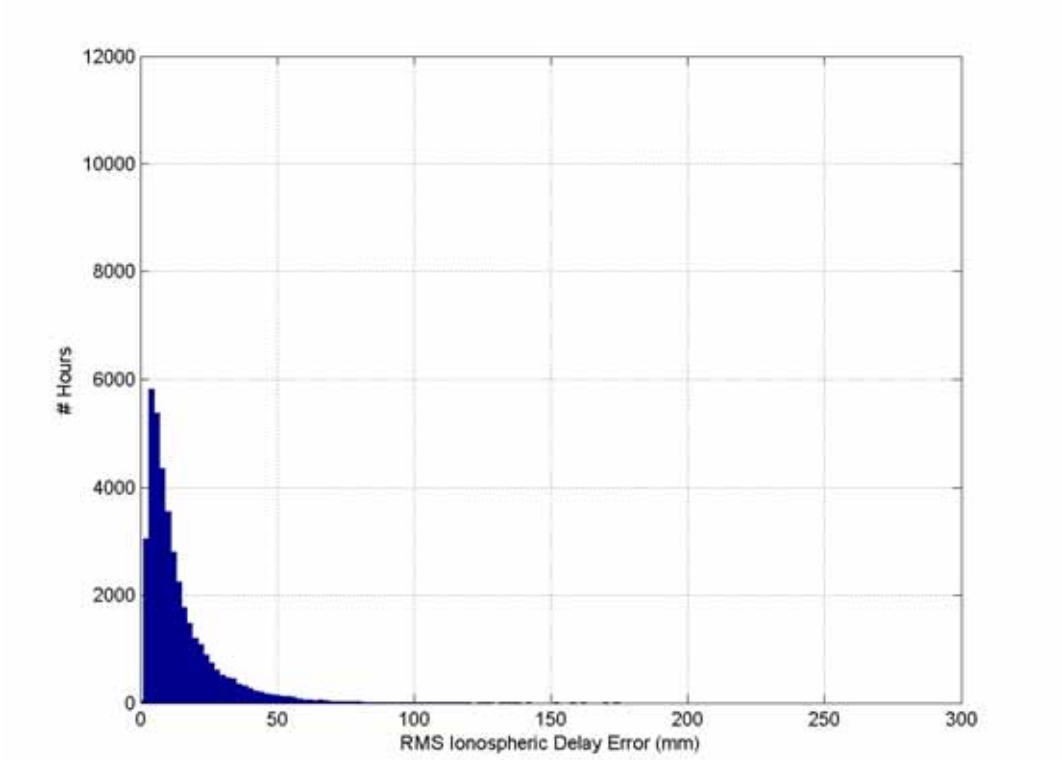

Figure 13 **Histogram over the L1 ionospheric interpolation error over North Triangle. Values are hourly errors.**

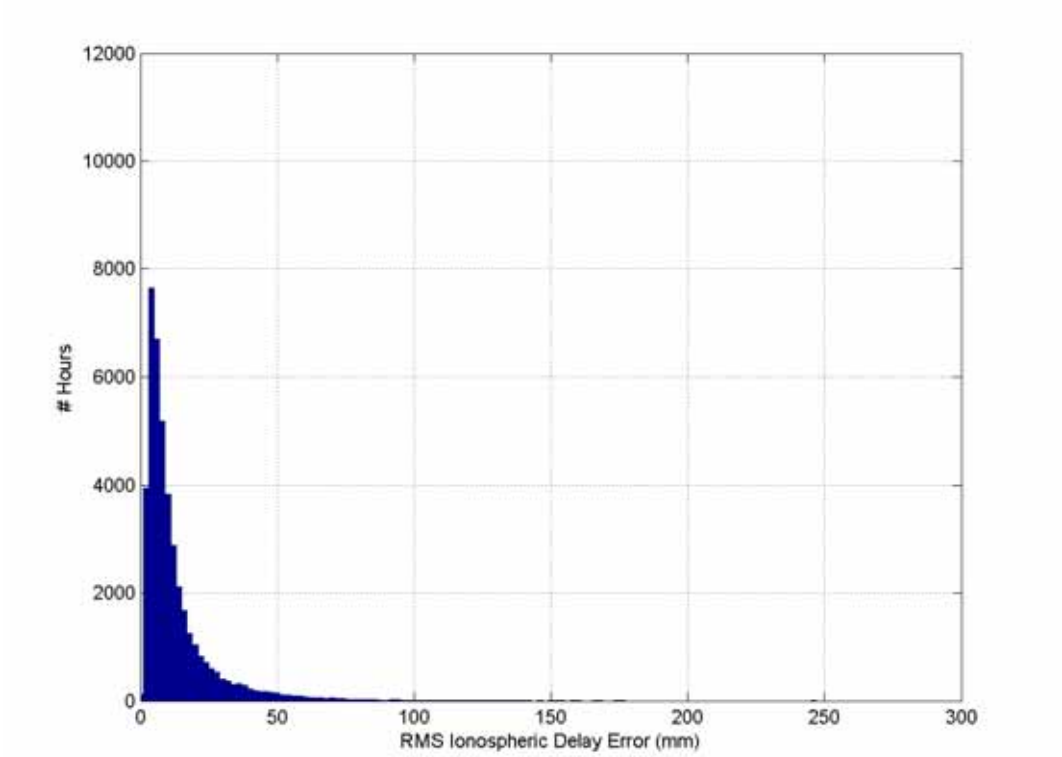

Figure 14 **Histogram over the L1 ionospheric interpolation error over Mid Triangle. Values are hourly errors.**

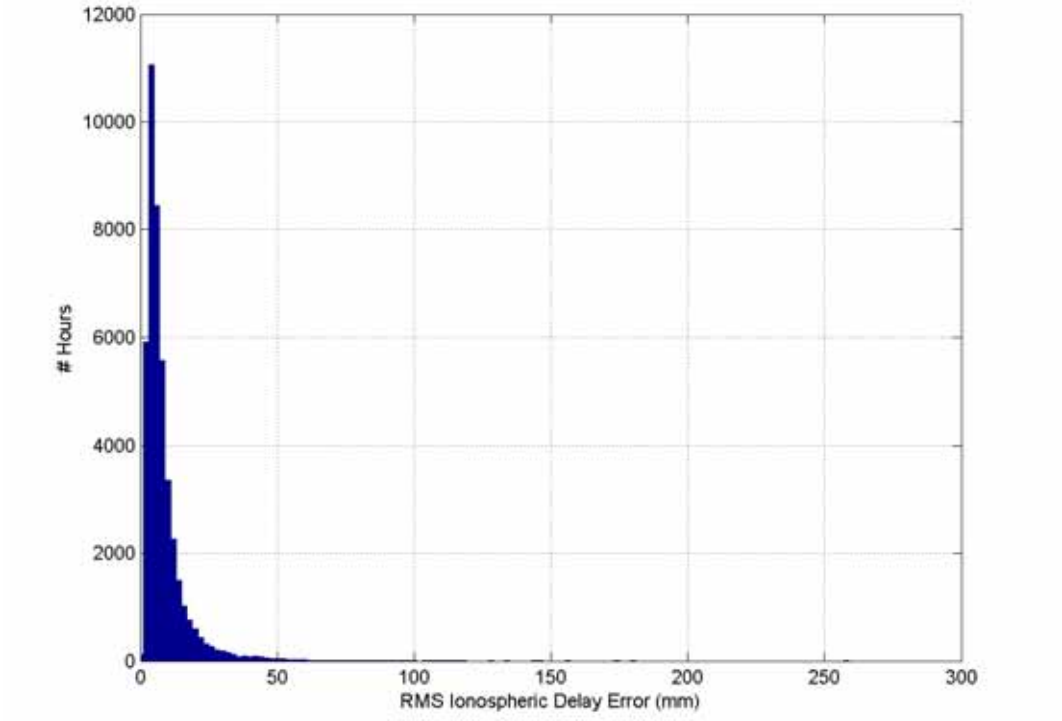

Figure 15 **Histogram over the L1 ionospheric interpolation error over South Triangle. Values are hourly errors.**

Table 2 shows the ionospheric variability in numbers for all triangles, North Triangle, Mid Triangle and South Triangle.

Table 2 Ionospheric variability for all triangles, North Triangle, Mid Triangle and South Triangle. The results reflect the five year study period and show rms values, 50th (median), upper 90%, upper 95%, upper 99% and upper 99.9%.

	Variability (mm)					
	RMS	**50%**	**90%**	**95%**	**99%**	**99.9%**
Total	17.1	7.5	24.9	35.6	63.5	112.8
North	19.3	9.5	30.2	40.3	65.3	105.8
Mid	19.1	8.1	27.6	39.6	72.6	130.2
South	12.2	6.0	16.1	22.6	45.5	88.8

Figure 16 shows the ionospheric interpolation error over North Triangle versus interpolation error over Mid Triangle. A clear correlation exists although there are significant differences between the interpolation errors in the two triangles. This indicates that when monitoring the ionosphere and its influence on network-RTK performance it is desirable to have several different geographical regions under observation. The effects in northern Sweden may, for example not be that relevant for a user in southern Sweden.

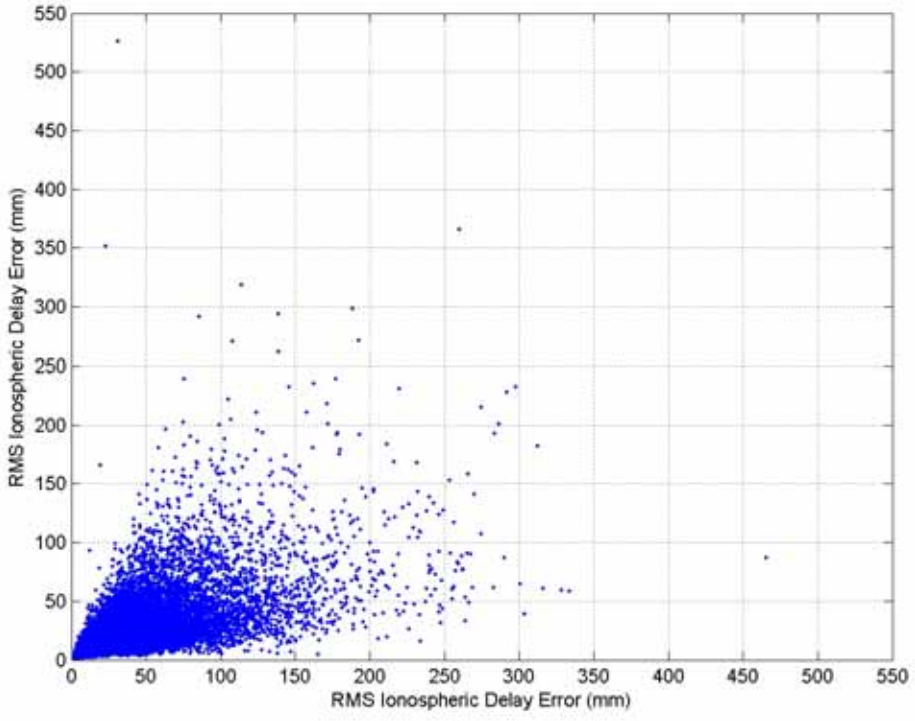

Figure 16 Ionospheric interpolation error over North Triangle versus interpolation error over Mid Triangle.

Figure 17 and Figure 18 show the ionospheric interpolation error versus TEC for North Triangle and Mid Triangle. There is a correlation between interpolation error and TEC, although not very strong. This indicates that a high TEC value is not necessarily a good indicator for problems with RTK-measurements. It also indicates that periods with low

TEC values and large ionospheric spatial variability occur during solar maxima, which result in potential problems for network-RTK users, see section 3.2 and 3.3.

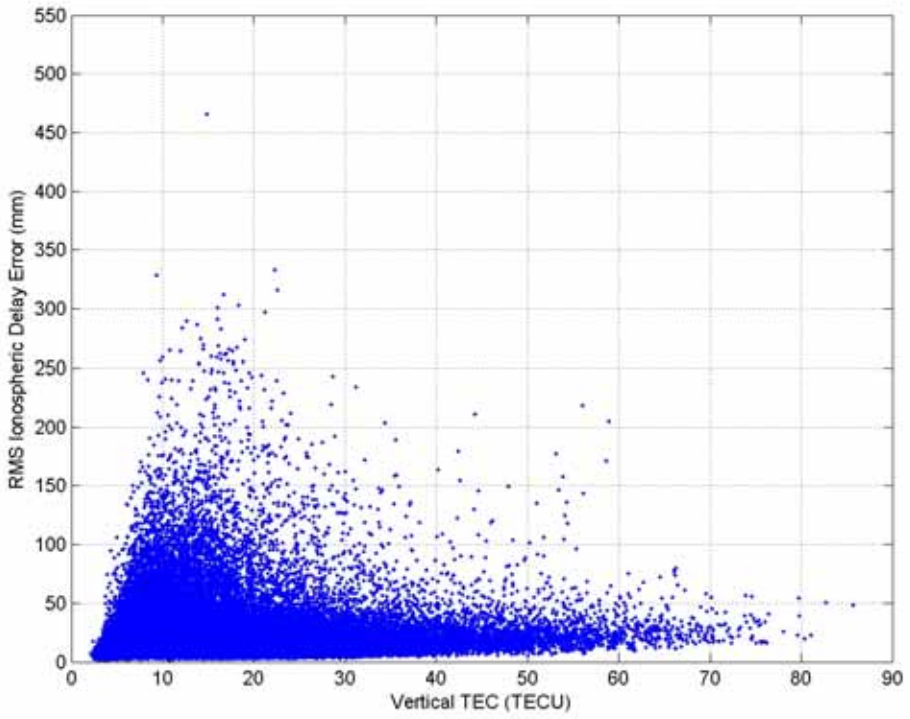

Figure 17 Ionospheric interpolation error over North Triangle versus TEC.

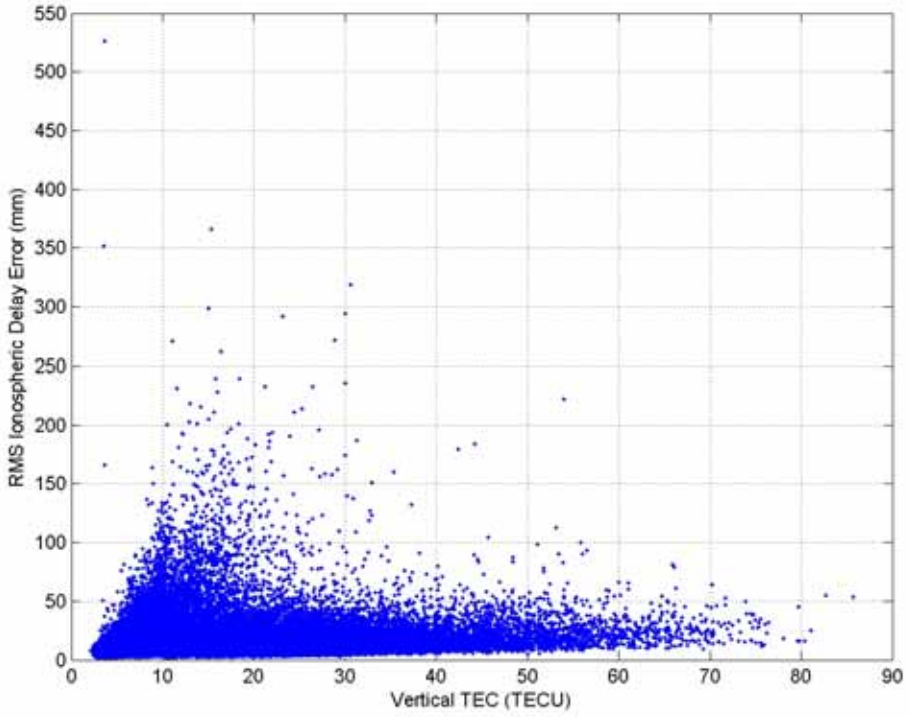

Figure 18 Ionospheric interpolation error over Mid Triangle versus TEC

Figure 19 shows the ionospheric interpolation error as a function of the time of the day for the three triangles. It is interesting to note that the most problematic part is usually

during night time. It is also clear that the interpolation errors are larger for the two northern triangles. This is especially true during night time.

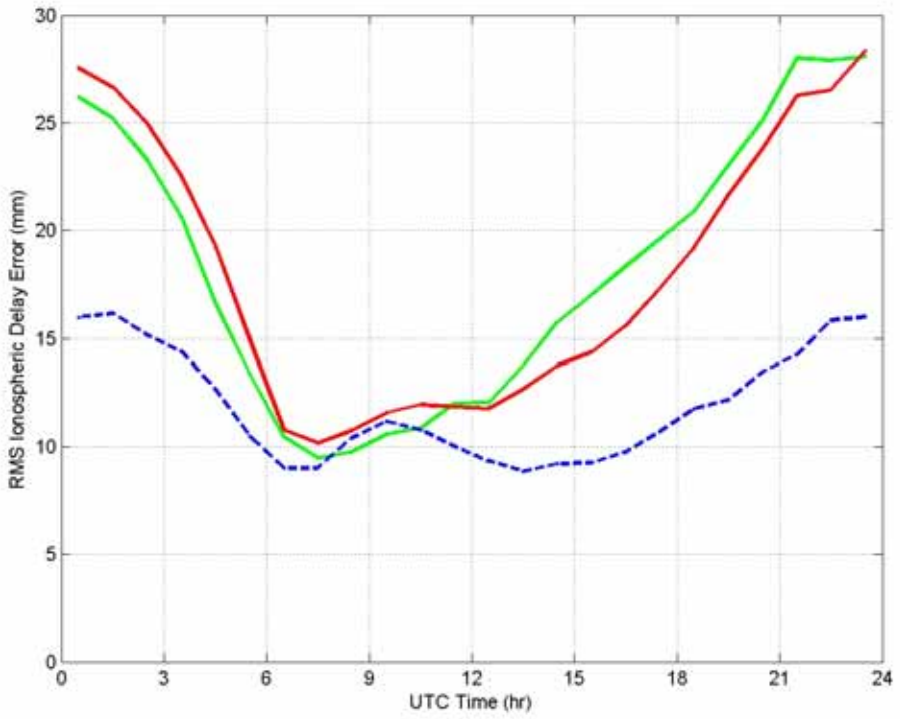

Figure 19 **Ionospheric interpolation error as a function of the time of the day, local time is CET. Errors from North Triangle are shown in green (solid line) , errors from Mid Triangle in red (solid line) and errors from South Triangle in blue (dashed).**

Figure 20 shows the ionospheric interpolation error as a function of season for the three triangles. The interpolation error is largest in October and November and smallest in June and July. The pattern is similar for all the three geographical areas studied in the report.

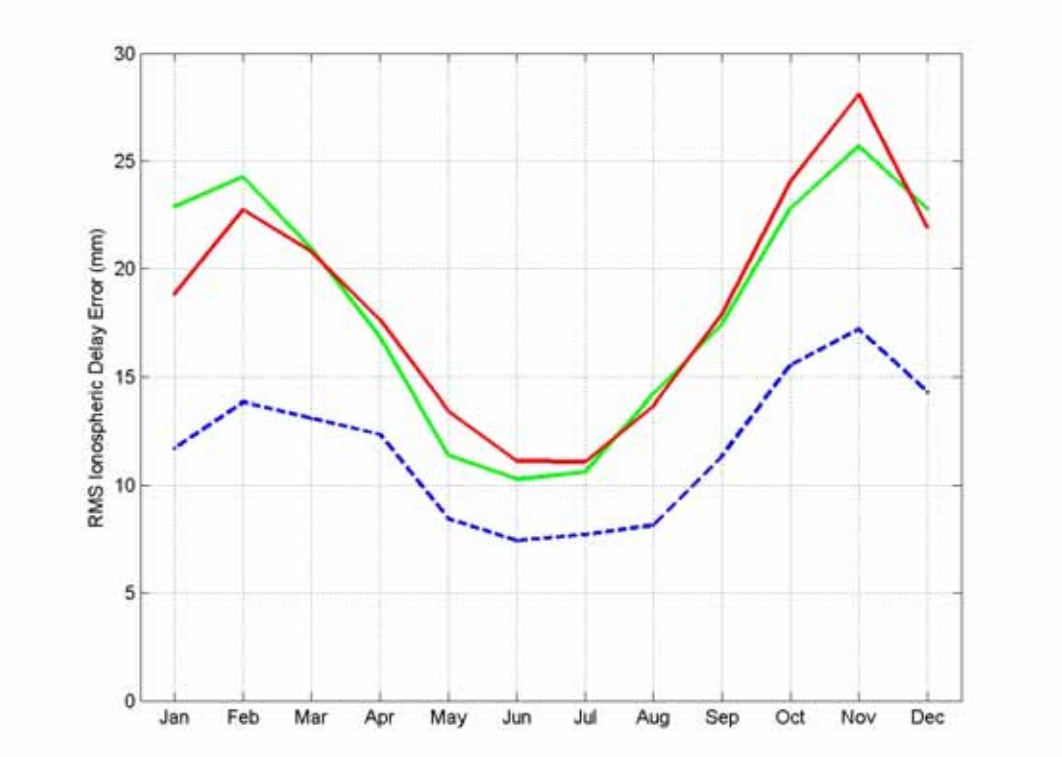

Figure 20 **Ionospheric interpolation error as a function of month. Errors from North Triangle are shown in green (solid line), errors from Mid Triangle in red (solid line) and errors from South Triangle in blue (dashed).**

2.4 Temporal Characterization

Rapid temporal variations or irregularly structured areas in the ionosphere can cause diffraction and scattering of signals that propagate through the areas where these occur. A signal received by the GPS antenna can present temporal fluctuations in both amplitude and phase. This is known as ionospheric scintillation. The effect may cause problems such as signal power fading, phase cycle slips, and receiver loss of lock.

Scintillation occurs as a result of variations in the refractive index of the medium through which waves are travelling. The variations in the refractive index is caused by variations in the concentration of particles, i.e., electrons and protons in the solar wind. Different indices of refraction in different areas result in phase changes between waves travelling through the different areas, which results in interference. As the waves interfere the intensity of the signal varies.

Figure 21 shows a scintillation map with the frequency of disturbances due to scintillations during solar maximum. It is clear that most scintillations occur around the equator, and also more frequently in pole ward than mid-latitudes.

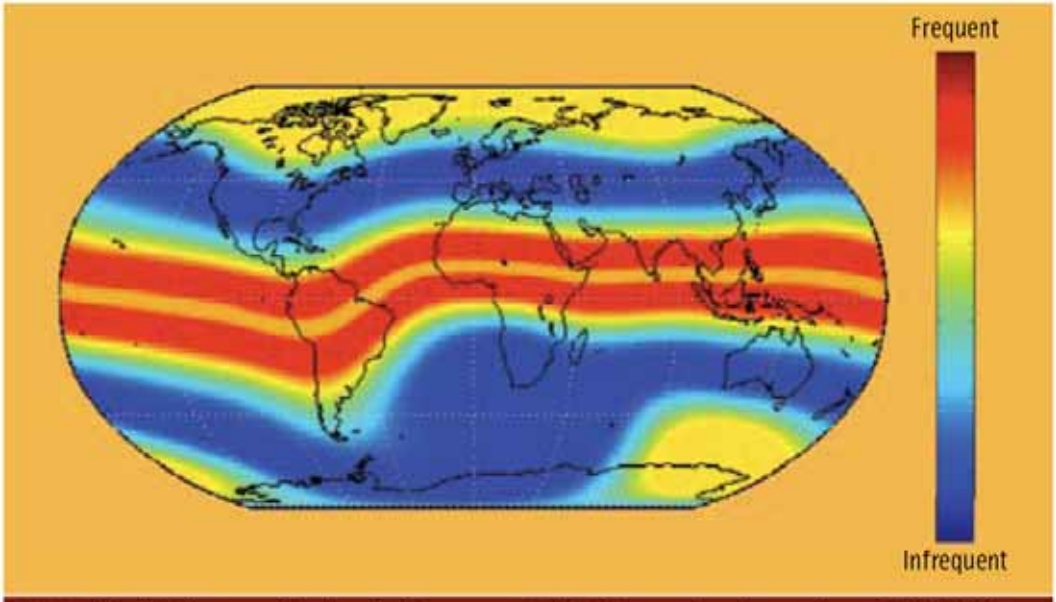

FIGURE 1 Scintillation map showing the frequency of disturbances at solar maximum. Scintillation is most intense and most frequent in two bands surrounding the magnetic equator, up to 100 days per year. At poleward latitudes, it is less frequent and it is least frequent at mid-latitude, a few to ten days per year.

Figure 21 **Scintillation map. The colour coding show the frequency of disturbances due to scintillations during solar maximum. From *Kintner et al* [2009].**

Several models exist for describing these scintillation effects. Using the Rytov approach [*Umeki et al.*, 1977] we can write the power spectrum of the recorded amplitude as a function of scanning velocity, U, transmitted signal frequency f_t, modeled thickness of the irregularity layer, L, distance from the layer to the receiver, z, plasma frequency, f_p, wave number for the signal, k, and power spectrum of the electron density irregularities :

$$S_\chi(\nu) = \frac{\pi k^2 L}{4U}\left(\frac{f_p}{f_t}\right)^4 \int_{-\infty}^{\infty} F_F(q) S_{\Delta N}(2\pi\nu/v, \kappa_y, 0) d\kappa_y \tag{6}$$

where

$$q^2 = \frac{2\pi\nu}{U} + \kappa_y^2, \tag{7}$$

and

$$F_F(\kappa) = 1 - \frac{2k}{\kappa^2 L}\sin\left(\frac{\kappa^2 L}{2k}\right)\cos\frac{\kappa^2}{k}\left(z - \frac{L}{2}\right) \tag{8}$$

is the Fresnel filtering function and the power spectrum of the electron density irregularities is

$$S_{\Delta N}(\kappa_x, \kappa_y, 0) = \frac{\eta\left\langle(\Delta N / N_0)^2\right\rangle \Gamma(p/2)}{\pi^{3/2}\Gamma[(p-3)/2]\kappa_0^3}\left(1 + \frac{\kappa_x^2 + \eta\kappa_y^2}{\kappa_0^2}\right)^{-p/2} \tag{9}$$

where η is the anisotropy factor for the irregularities, $\langle(\Delta N/N_0)^2\rangle$ is the variance of the electron density fluctuations, p is a power law exponent, Γ is the gamma function, and κ_0

is the outer scale wave number. Detailed description of the scintillation phenomena and the described parameters can be found in *Yeh and Liu* [1982].

Figure 22 shows the power spectrum of satellite measurements at 40 MHz received with a stationary receiver in Boulder, USA [*Umeki et al.*, 1977]. Also in the figure is a theoretical power spectrum computed using the equations above. The used parameter values result in a good agreement between the measurements and the model.

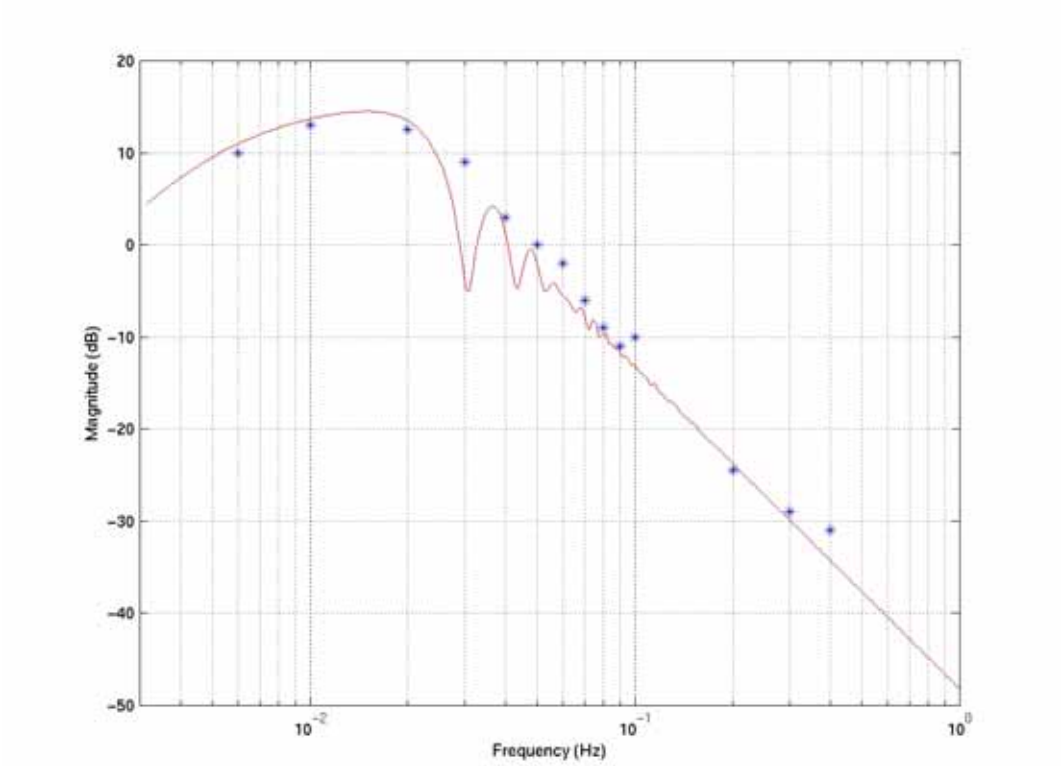

Figure 22 **Amplitude spectrum of observations made at 40 MHz (blue stars) and model values from Umeki (red line).**

Figure 23 shows amplitude spectrum for GPS L1 signals based on the Umeki model and the same parameter values as used for the measurements on 40 MHz. Such models will be used to generate relevant signals in order to study GNSS receiver ability to track signals under difficult ionospheric conditions.

In order to simulate the influence of ionospheric scintillations on the ability of GPS receivers to track the received signals we define two different scenarios, which are described in section 3.1.

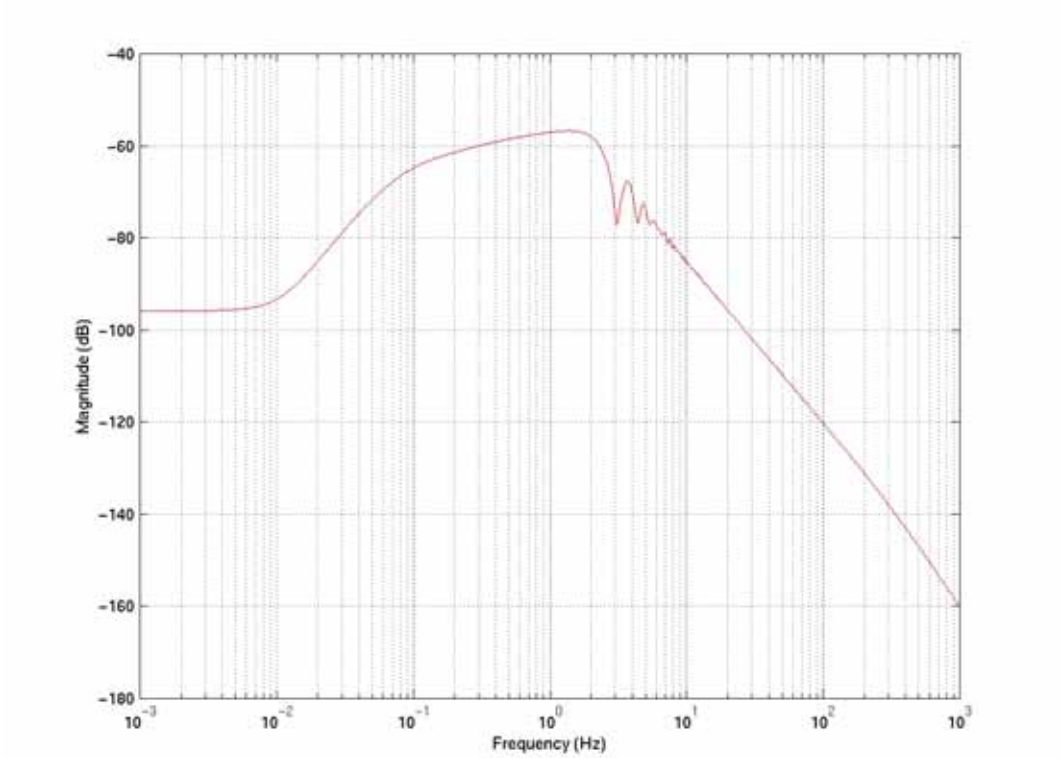

Figure 23 Amplitude spectrum for GPS L1 signals based on the Umeki model.

2.5 Statistics from GNSS data

Large ionospheric temporal variations may lead to receiver problems with, for example, frequent cycle slips. Cycle slips both at reference and rover receivers cause problems for users of network-RTK, such that observations from a slipping satellite becomes useless for a period of time.

We have used GPS data from the focus period in order to investigate how frequently cycle slips occur during the period. In this report by a cycle slip we mean that the difference between two temporally adjacent L4 phase measurements is more than 20 cm. If a cycle slip occurs for any of the receivers in a triangle during a period, we refer to this specific satellite observation as a "slipping satellite".

Figure 24, Figure 25, and Figure 26 show the number of slipping satellites in each 1 hour period during the five years at North Triangle, Mid Triangle and South Triangle respectively. It is important to note that the reported number of cycle slips are based on the equipment used at the time of the focus period. We anticipate improvement in the receivers' ability to follow rapid signal variations during the next solar cycle.

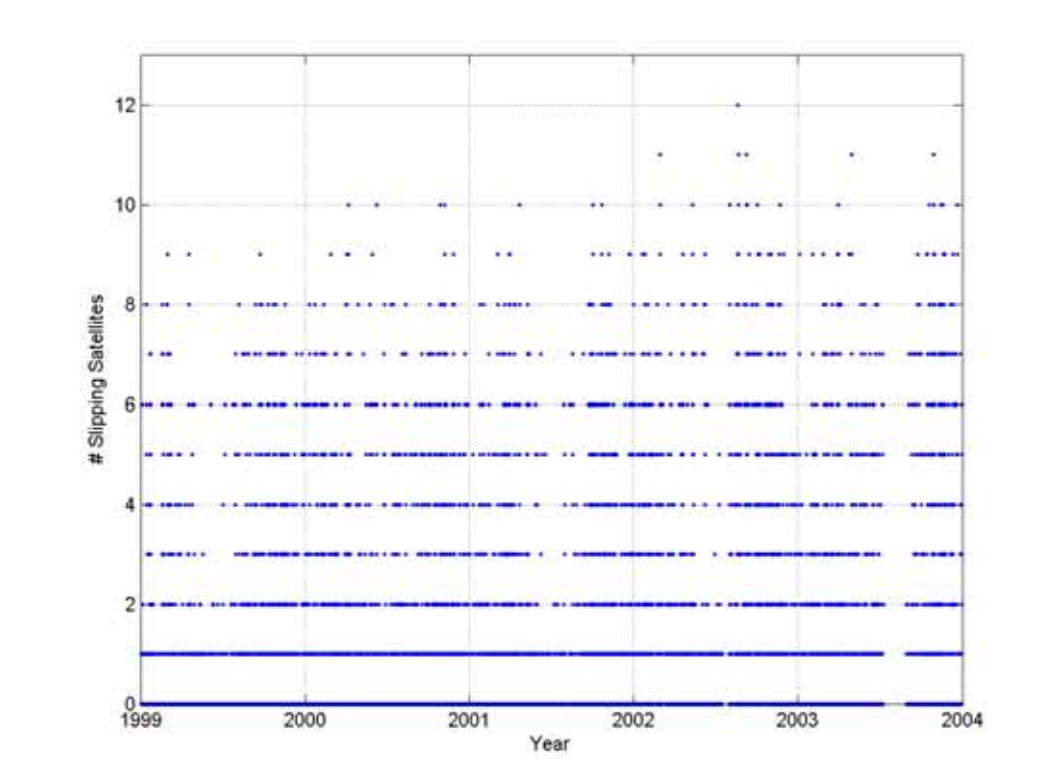

Figure 24 **Number of slipping satellites per hour during five years at North Triangle.**

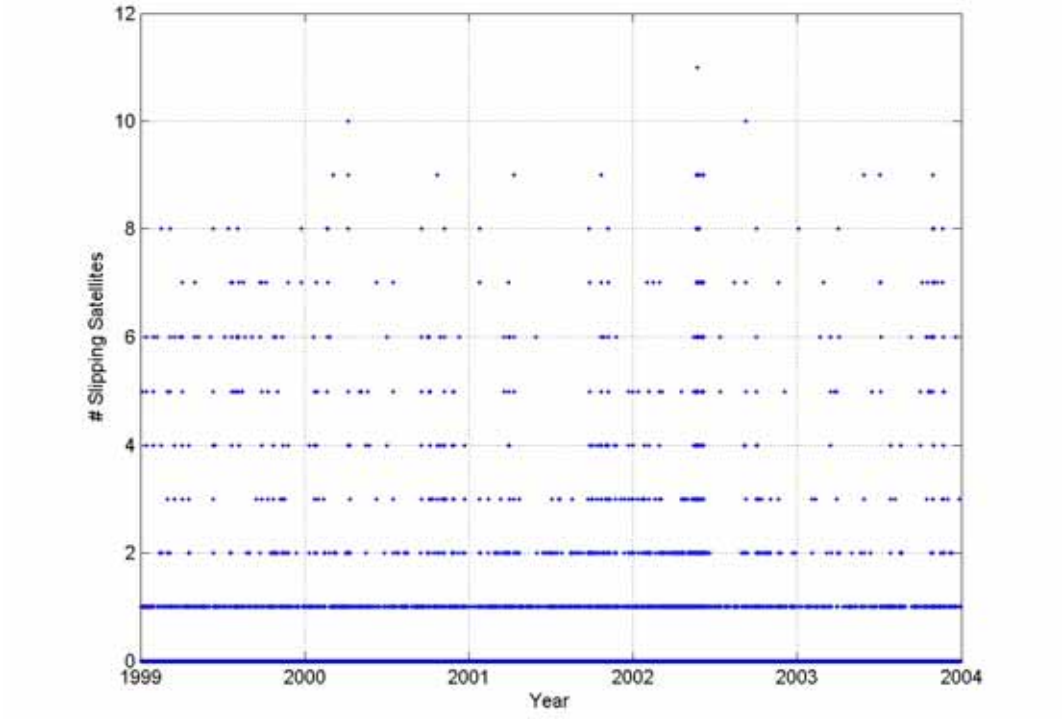

Figure 25 **Number of slipping satellites per hour during five years at Mid Triangle.**

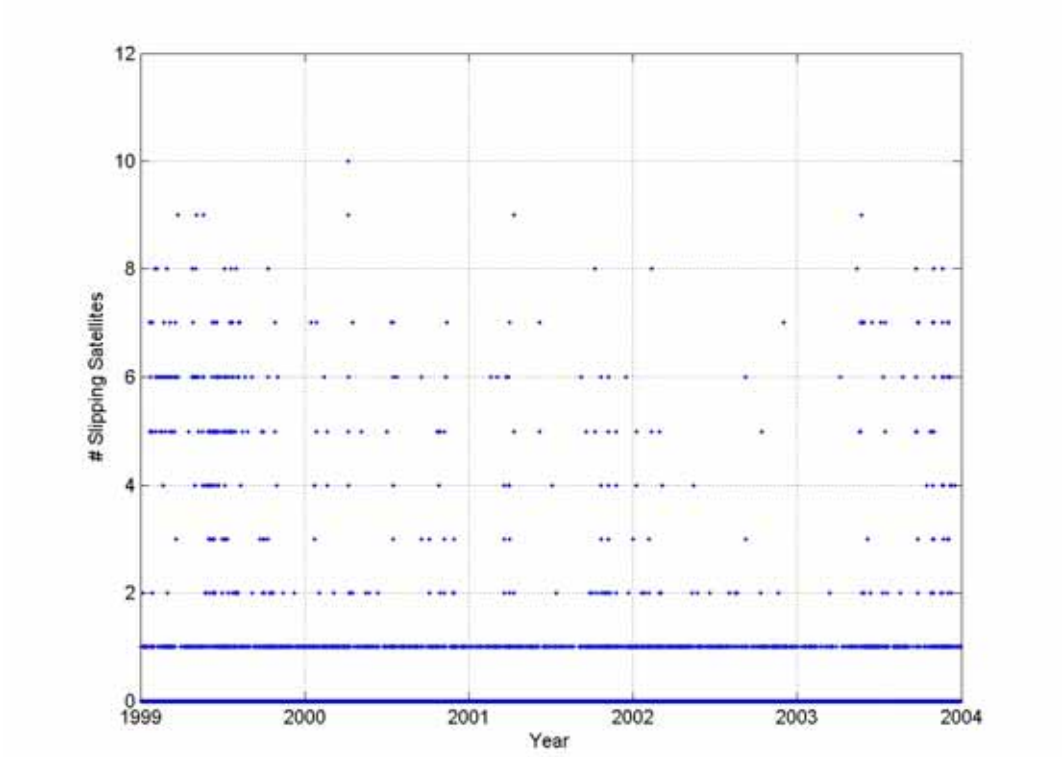

Figure 26 Number of slipping satellites per hour during five years at South Triangle.

Figure 27, Figure 28 and Figure 29 show the histogram over the amount of slipping satellites per hour for North Triangle, Mid Triangle and South Triangle respectively.

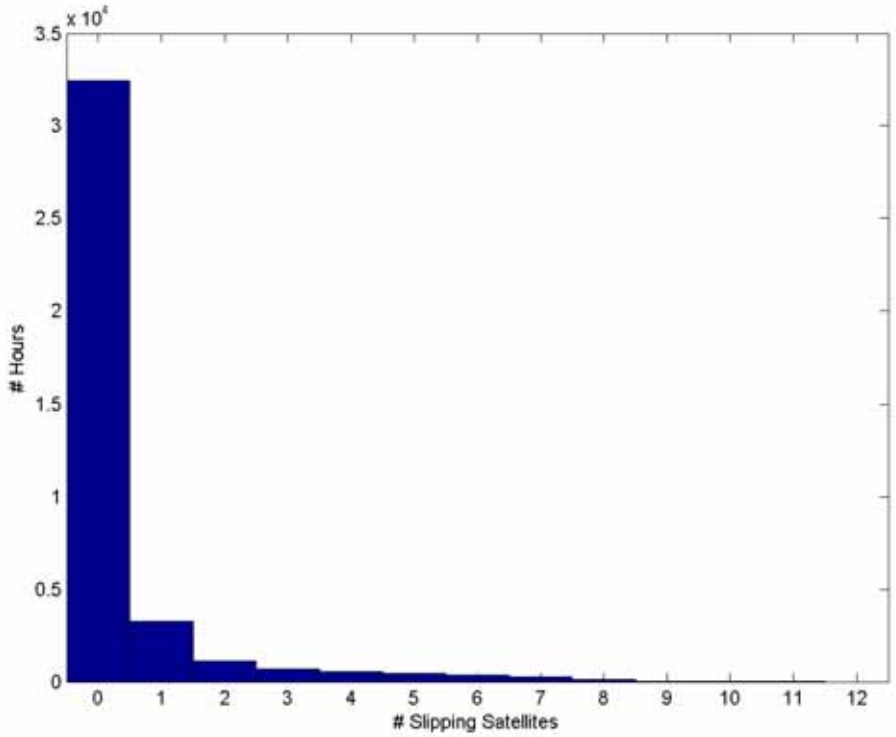

Figure 27 **Histogram over number of slipping satellites per hour during five years at North Triangle.**

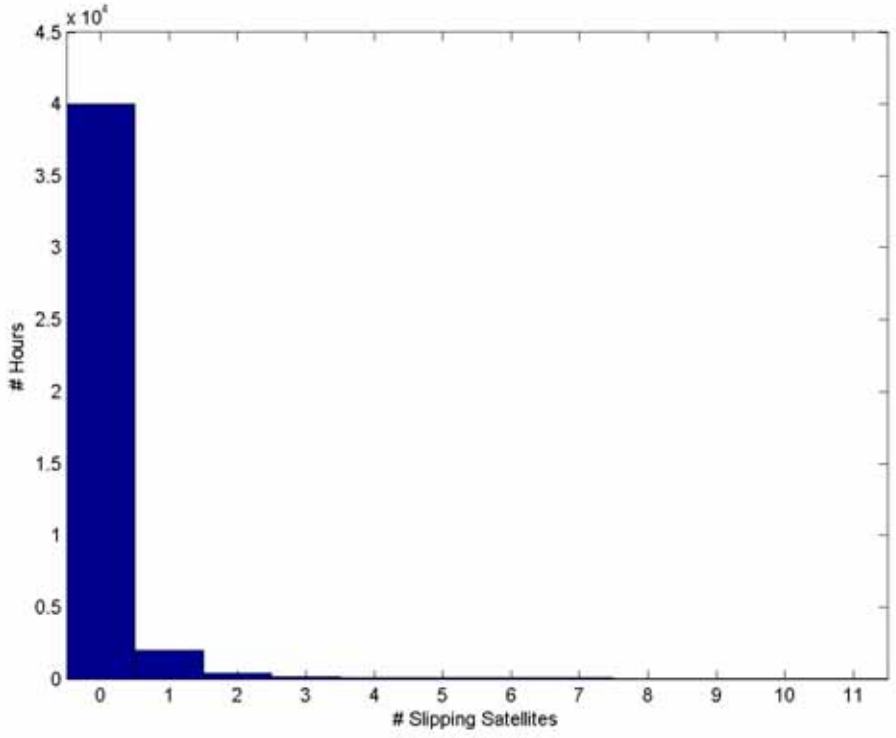

Figure 28 **Histogram over number of slipping satellites per hour during five years at Mid Triangle.**

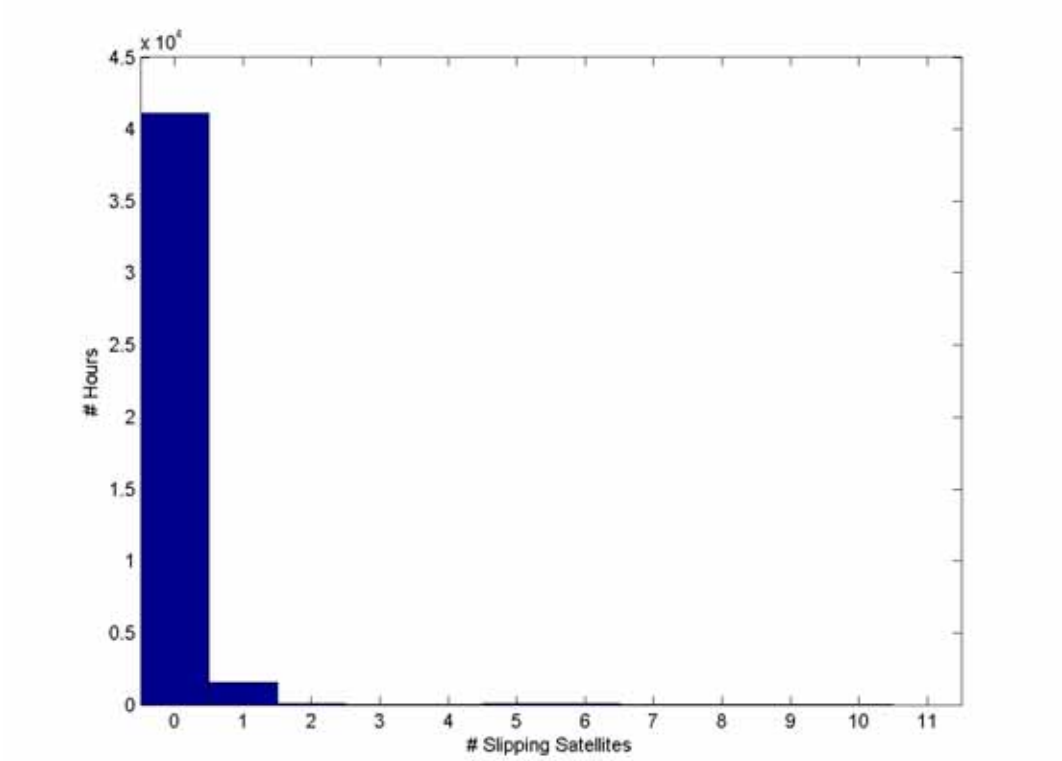

Figure 29 **Histogram over number of slipping satellites per hour during five years at South Triangle.**

Figure 30 shows the amount of slipping satellites as a function of the time of the day for the three triangles. From the figure it is clear that the number of slips are larger in the more northern triangles. This is in agreement with the scintillation map in Figure 21 which predicts higher frequency of scintillations in more northern areas and subsequently more phase slips. There is a very large difference also between the number of slipping satellites between the mid and north triangle. A part of this large difference is presumably due to differences in instrumentation.

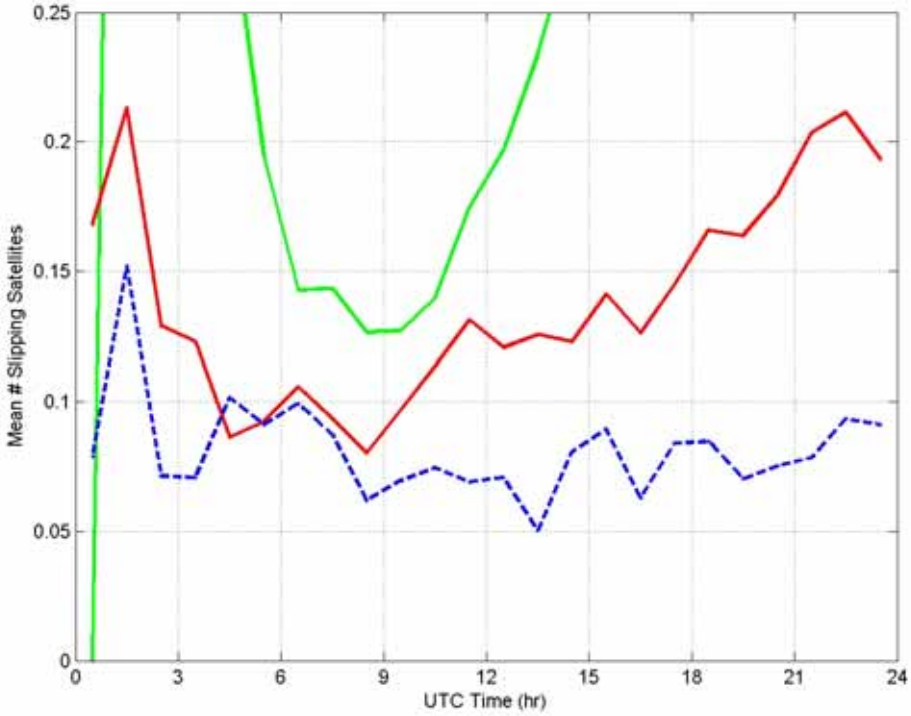

Figure 30 **Number of slipping satellites as a function of the time of the day. Slips in North Triangle are shown in green (solid line) , slips in Mid Triangle in red (solid) and slips in South Triangle in blue (dashed). For clarity the y-axis is adjusted to fit results from Mid Triangle and South Triangle.**

Figure 31 shows the number of slipping satellites as a function of the ionospheric interpolation error. The figure shows that there is a clear correlation between the spatial variability causing the interpolation errors and the cycle slip occurrence caused by scintillation phenomena.

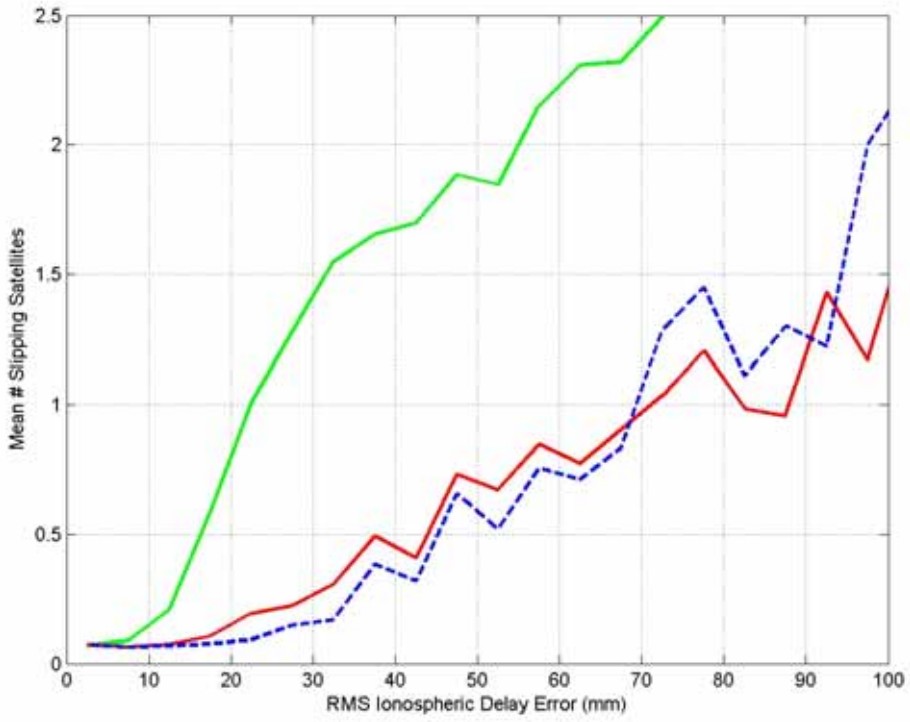

Figure 31 **Number of slipping satellites as a function of the ionospheric interpolation error. Results from North Triangle are shown in green (solid line), from Mid Triangle in red (solid) and from South Triangle in blue (dashed).**

Figure 32 shows an example of data behind the statistics in this section of the report. The figure shows the number of slipping satellites, the ionospheric delay interpolation error, and the TEC for Mid Triangle during one week of observations. Data is from day 299 to day 305, 2000, which was a period with extreme ionospheric activity.

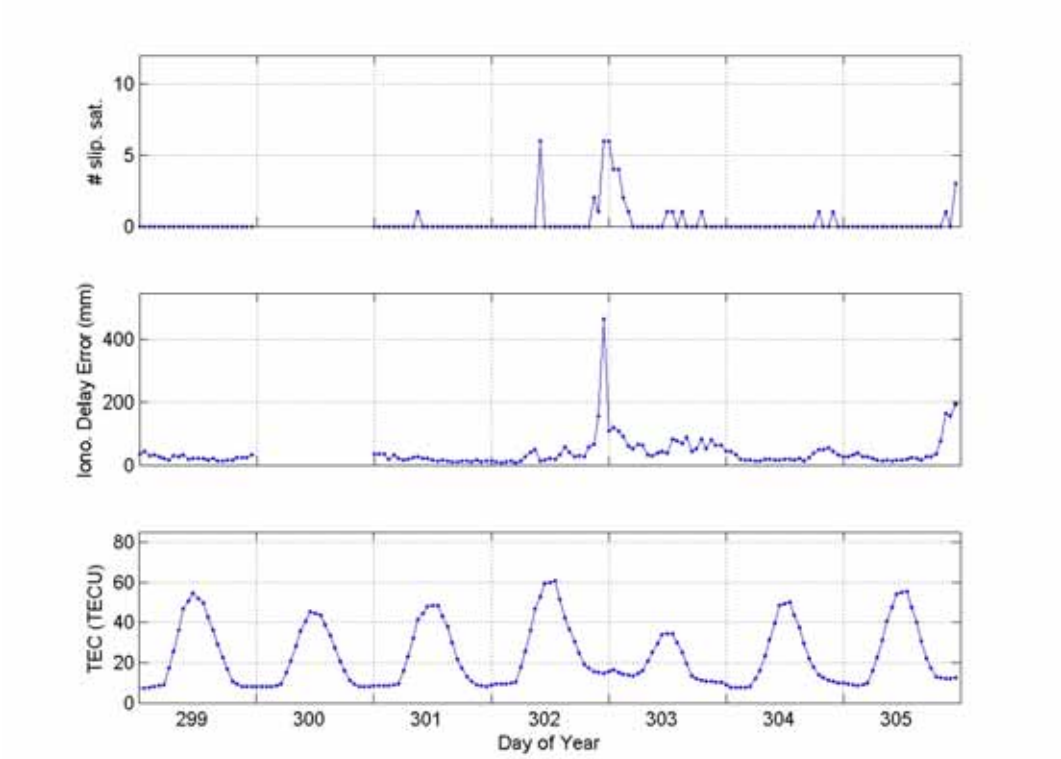

Figure 32 **Example of hourly results for a one week period. The upper panel shows the number of satellite slips. The middle panel shows the mean ionospheric delay interpolation error, and the lower panel shows the TEC.**

2.6 Reported user experience

Based on the recorded user feedback of the network-RTK performance during the previous solar maximum, we obtain an indication on the level of problems caused by ionospheric activity. Figure 33 shows statistics based on reported user problems assumed to be due to ionospheric activity during our focus period. We can see that the number of registered problems increased during the first five years. However, the number of users also increased during this time period so it is reasonable to expect also an increase in the number of reported problems. It is interesting to note, though, that the number of problems decreased after 2005 in spite of a still increasing number of users.

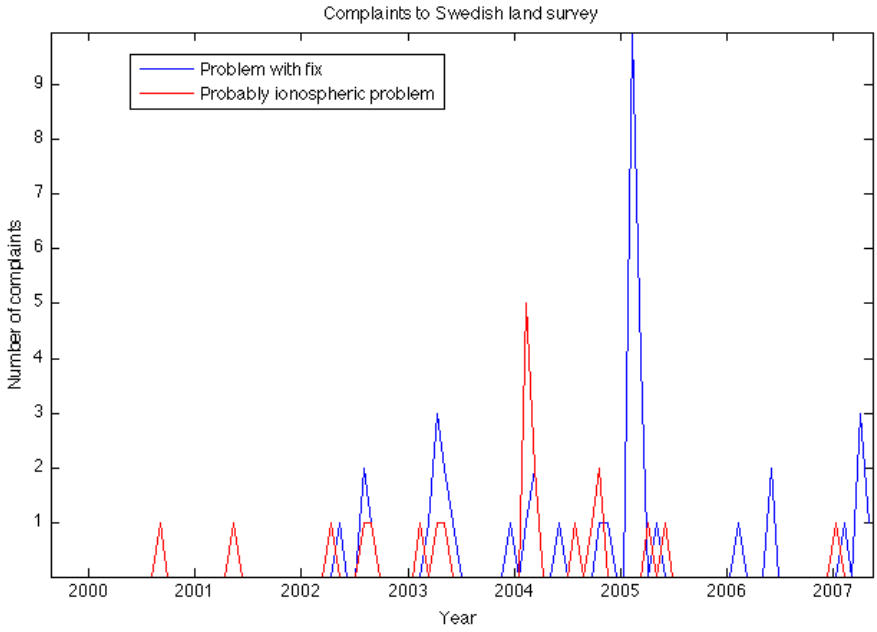

Figure 33 Number of Network-RTK user problems.

3 GNSS reception

3.1 Scintillations

In order to simulate the influence of ionospheric scintillations on the ability of GPS receivers to track the received signals we define two different scenarios. Table 3 specifies the model parameters chosen for the two scenarios. See section 2 for an explanation of the different parameters. We have chosen the parameter values based on different studies of the ionosphere presented in the literature. Both scenarios contain high values on the electron density variability, e.g., *Umeki et al.* [1977]. The difference between the two scenarios is the parameter representing the outer scale wavenumber. Scenario 1 is based on an outer scale wavenumber of 0.31 km found in *Basu et al.* [1976], whereas scenario 2 is based on an outer scale wave number of 7.8 km. Based on these and the equations (6-9) we can calculate spectra for the phase and amplitude variations. Figure 34 shows the amplitude spectrum for the two scenarios together with standard case based on measurements on 40 MHz as illustrated in Figure 23. It is worth noticing that signals based on Scenario 2 have more energy in the higher frequency regions than those in Scenario 1. Figure 35 shows the spectrum for the signal phase variations. Also here we can note that Scenario 1 will be subject to signals that contain more low frequency variations than do Scenario 2.

Table 3 Parameters defining Scenario 1 and Scenario 2.

	Scenario 1	**Scenario 2**
P	4	4
L (km)	200	200
U (m/s)	800	800
κ_0 (m^{-1})	$3.1 \cdot 10^{-4}$	$7.8 \cdot 10^{-4}$
η	1	1
$\sigma_{\Delta N}$ (m^{-3})	$3 \cdot 10^{11}$	$3 \cdot 10^{11}$

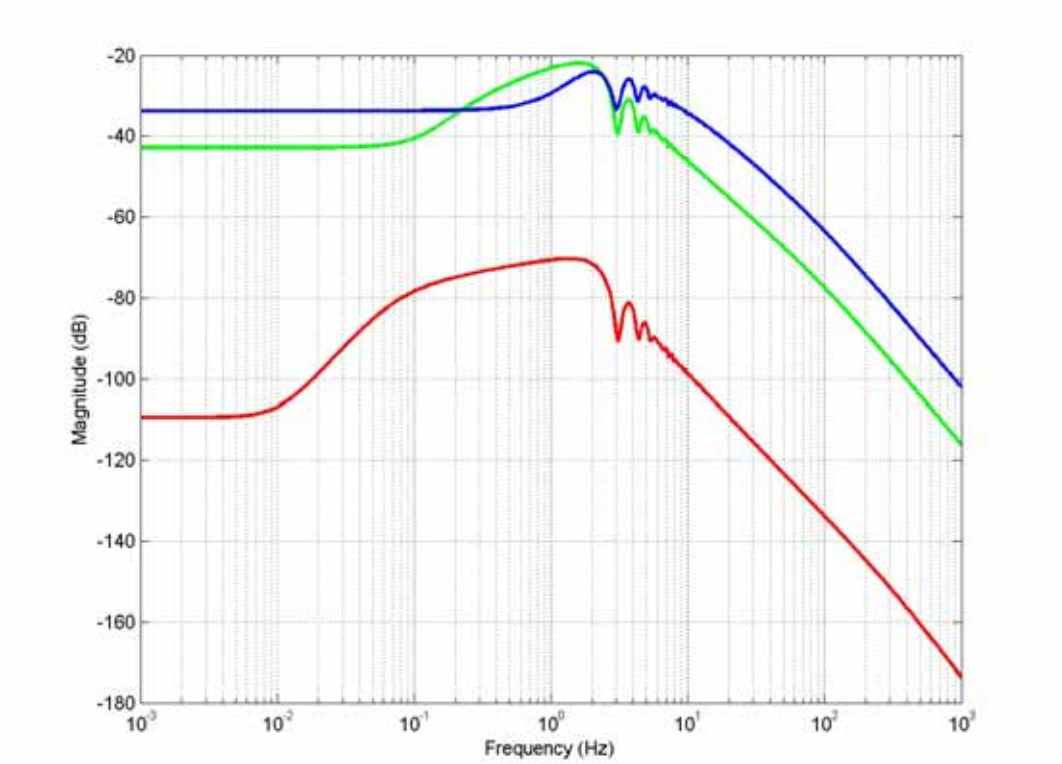

Figure 34 **Amplitude spectrum for Scenario 1 (green) Scenario 2 (blue) together with a nominal situation (red).**

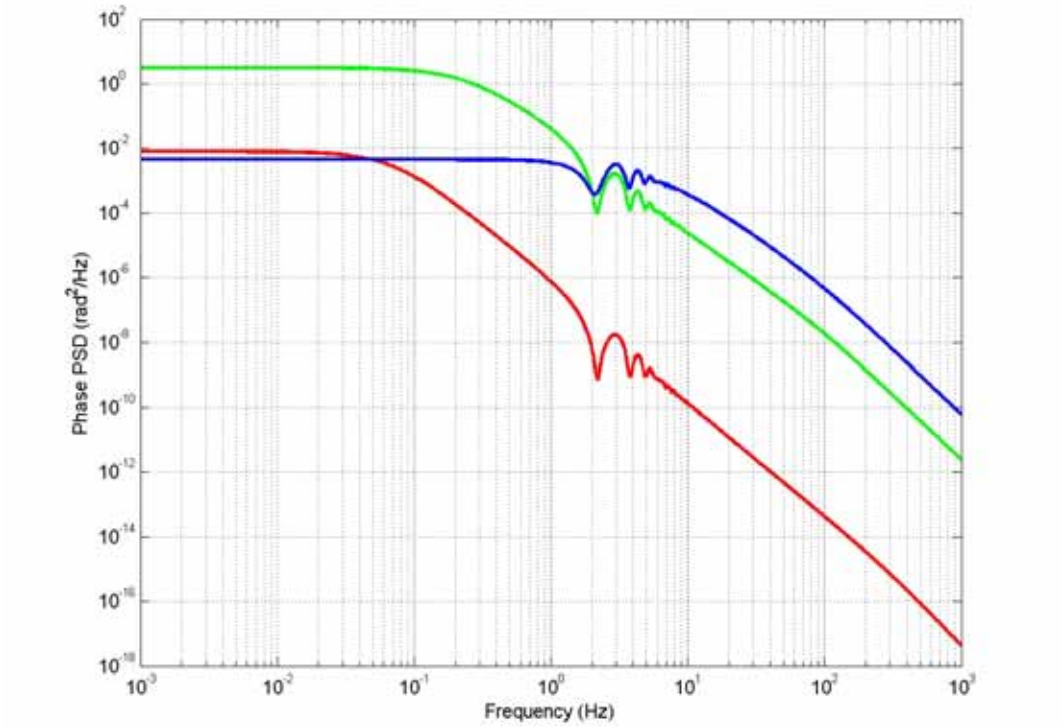

Figure 35 **Phase spectrum for Scenario 1 (green) Scenario 2 (blue) together with a nominal situation (red).**

Given the amplitude and phase spectra for the two scenarios, we can simulate signal amplitude and phase variations. We use the spectra in order to produce several different time series of these variations. Figure 36 shows four generated time series of amplitude variations for Scenario 1. Each panel in the figure shows the relative amplitude variations of a received GNSS signal at the L1 frequency. The illustrated time period is 2 s long and contains 1000 values per second.

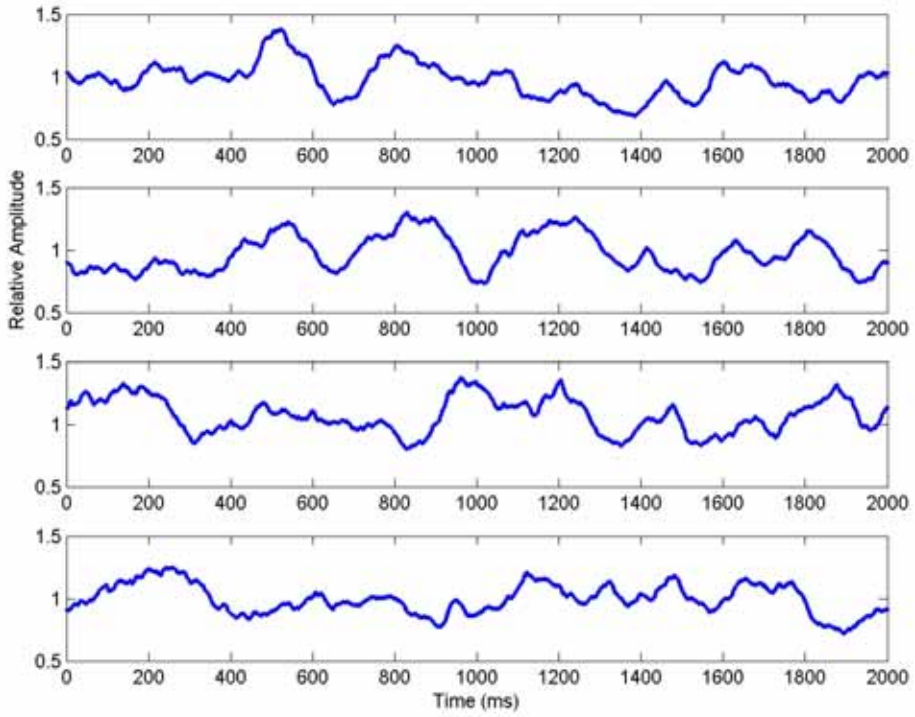

Figure 36 Simulated GNSS signal amplitude variations for scintillations based on Scenario 1.

Figure 37 shows the corresponding results for Scenario 2.

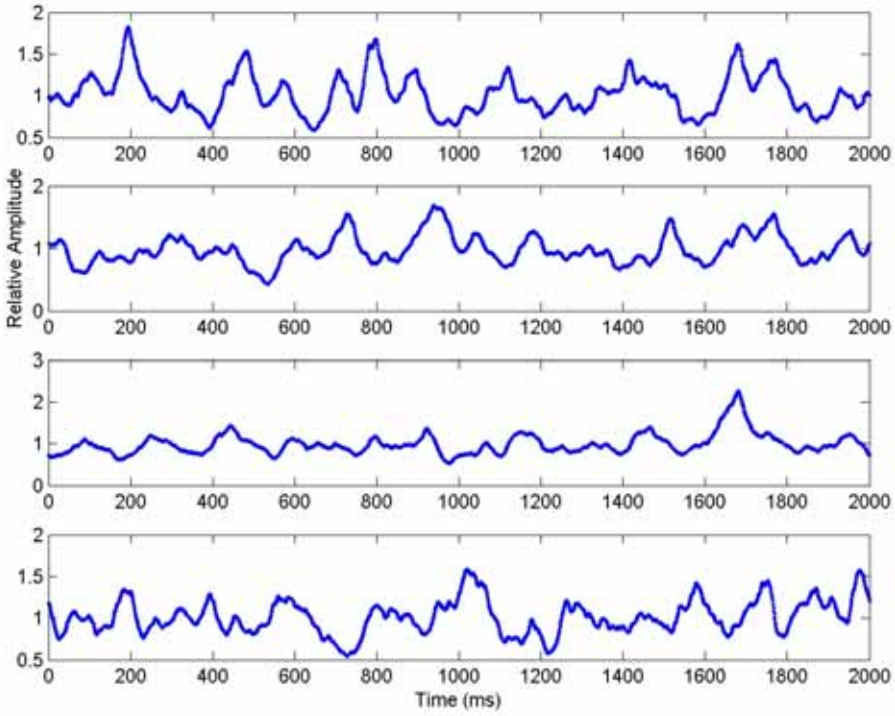

Figure 37 Simulated GNSS signal amplitude variations for scintillations based on Scenario 2.

Figure 38 and Figure 39 show the phase variations in radians for the two scenarios respectively. From the figures we can clearly see that Scenario 2 contains more rapid variations both in phase and amplitude, which was also expected from the spectra.

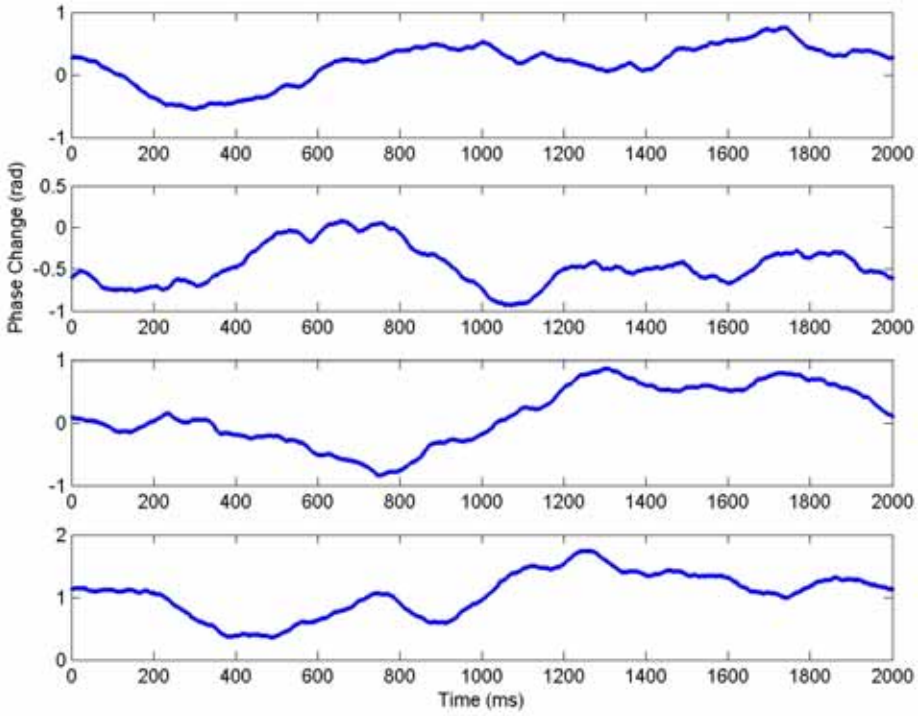

Figure 38 GNSS signal phase variations for scintillations based on Scenario 1.

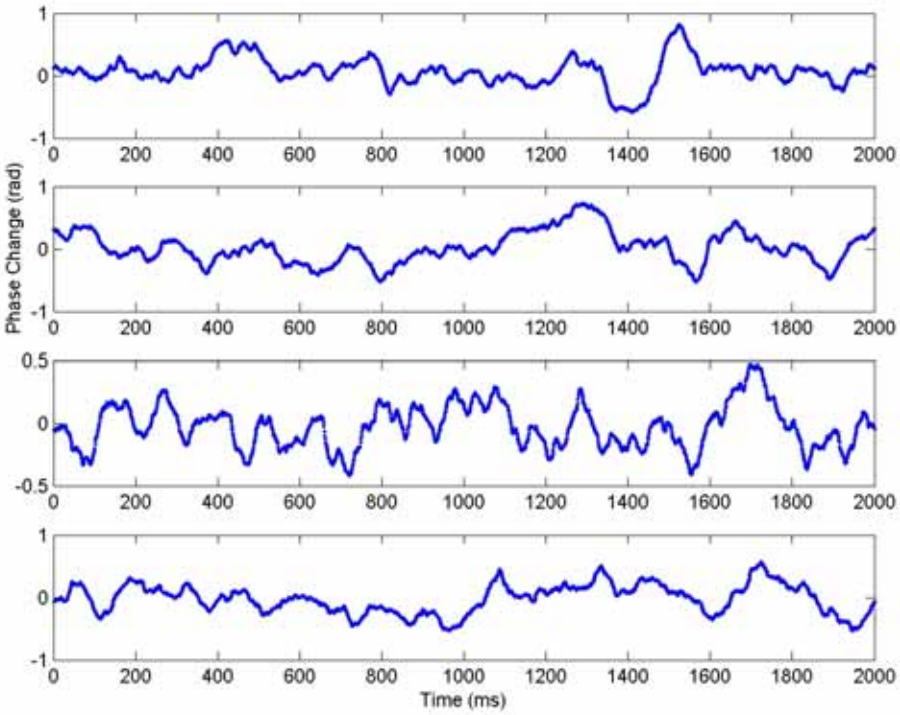

Figure 39 GNSS signal phase variations for scintillations based on Scenario 2.

3.2 Ambiguity fixing

High ionospheric spatial variability may constitute a problem for network-RTK measurements and the possibility to find the correct number of phase cycles, thus resolving the phase ambiguities. Problems may occur for users in different ways: The worst case is if the network-RTK software is unable to resolve the phase ambiguities or resolve the ambiguities incorrectly and thus is unable to produce a reliable measurement. Another situation is that the time it takes for the receiver to resolve the phase ambiguities and produce a measurement is much longer than normal.

In this section we study how well ambiguities are resolved and the time it takes under different ionospheric conditions. In order to perform the study, we use an experimental setup as shown in Figure 40 . Two GNSS receivers were used. Both receivers were connected to the same antenna. One of the receivers was used as the reference receiver and the other receiver was used as rover. The RTCM corrections from the reference receiver was sent to a PC. Before the messages were sent to the rover, we manipulated them by simulating different degrees of ionospheric contribution. That is, the ionosphere model provided by the computer adds an error to the RTCM data in order to simulate the effect of differences in the received data in the rover and the interpolated data that the network RTK software provides. For the experiment, we used a Javad Delta as simulated reference receiver and a Javad LEXON as simulated rover. The corrections were sent using both RTCM v2.3 and RTCM v3. This experiment gives an indication of how the situation can be under different ionospheric conditions. We should however remember that the results are representative for the currently used setup only and that most receivers have many different possibilities to deal with large ionospheric variability.

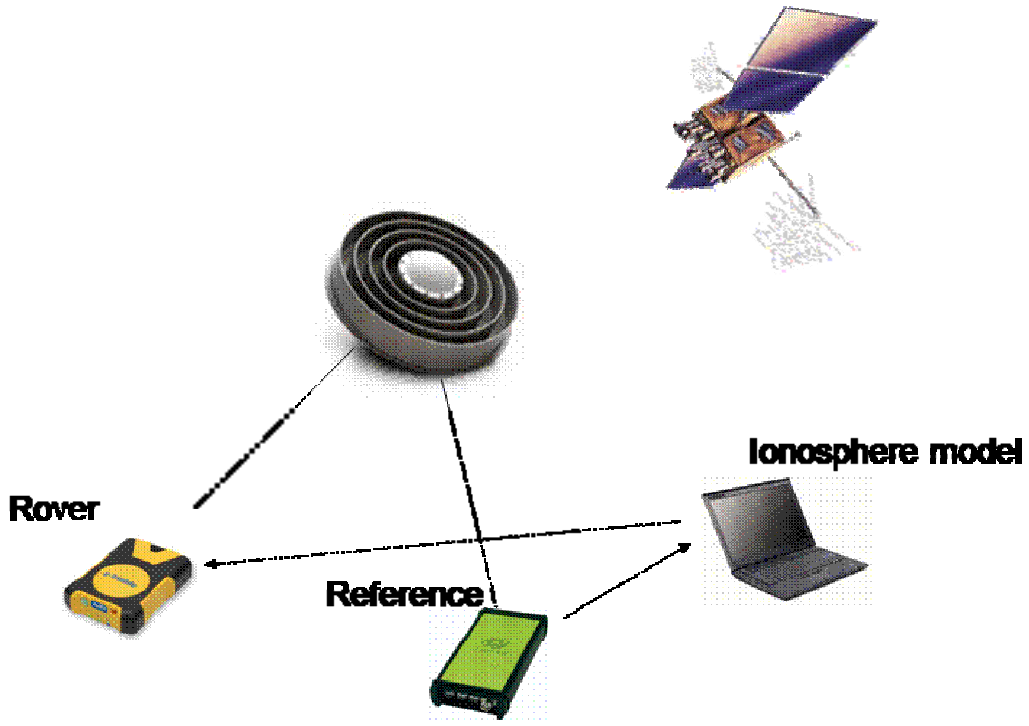

Figure 40 **Experimental setup for the study on ambiguity fixing during different ionospheric conditions.**

The interpolation errors in network-RTK due to ionospheric spatial variability are described in [*Emardson et al.*, 2009]. Statistically they can be described as Gauss Markov-processes with an autocorrelation A as:

$$A(\tau) = E\left[\varphi_D(t+\tau)\varphi_D(t)\right] \tag{10}$$

as

$$A = A_0 e^{\tau / t_c} \tag{11}$$

where t_c is the decorrelation time, set to 1000 s, and A_0 describes the variability of the process. In order to study the impact on network-RTK quality, we generate simulated time series of interpolation errors. We generate independent time series for each satellite that is observed. The timeseries are based on the autocorrelation function and mapped to the elevation angle to each satellite using the mapping function:

$$m_i(\varepsilon) = \frac{1}{\cos\left(\arcsin\left(\frac{R\sin(\varepsilon + \pi/2)}{R+h}\right)\right)} \tag{12}$$

where ε is the elevation angle of the observation, *R* is the radius of the earth and *h* is the height of the ionosphere, here represented as a thin shell. During a period the variability is constant. We vary the variability, i.e., the square root of A_0, in a cyclic sequence with the values 0, 2.5, 5, 7.5, 10, 15, 20, 30, 40, 50 mm. These values are relatively well representing the ionospheric variability found from the five year study period and shown in Figure 13, Figure 14, and Figure 15 for the three Swedish triangles.

In order to study the effect of the varying ionospheric variability, we repeated this sequence 232 times resulting in 232 measurements of the time to obtain a correct fix ambiguity solution as well as the position error for each investigated value. For each level of variability the rover tried to fix the ambiguities and estimate a position. Figure 41 shows the histogram of the time to fix for the case with the ionospheric variability set to zero. We can note that the main part of the results are to be found around 15 seconds which is reasonable for calm conditions. Figure 42 to Figure 50 show the histograms for the ionospheric variability of 2.5 to 50 mm.

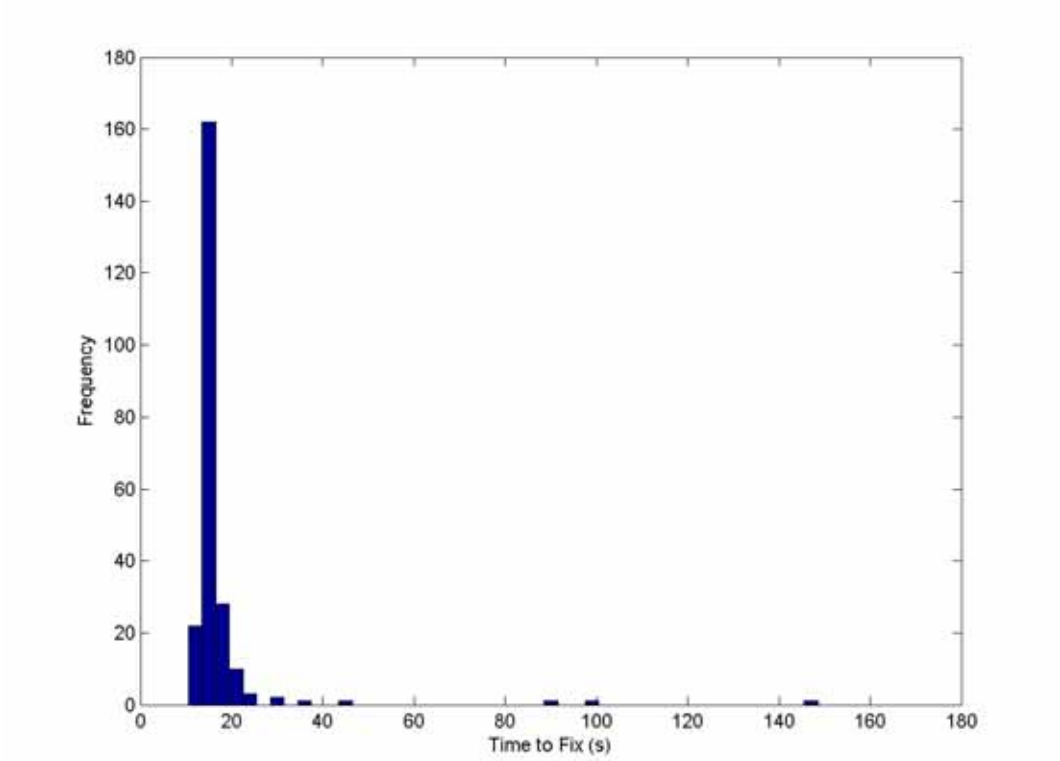

Figure 41 **Histogram over the time to fix, when there is no difference in the ionosphere between the reference and the rover.**

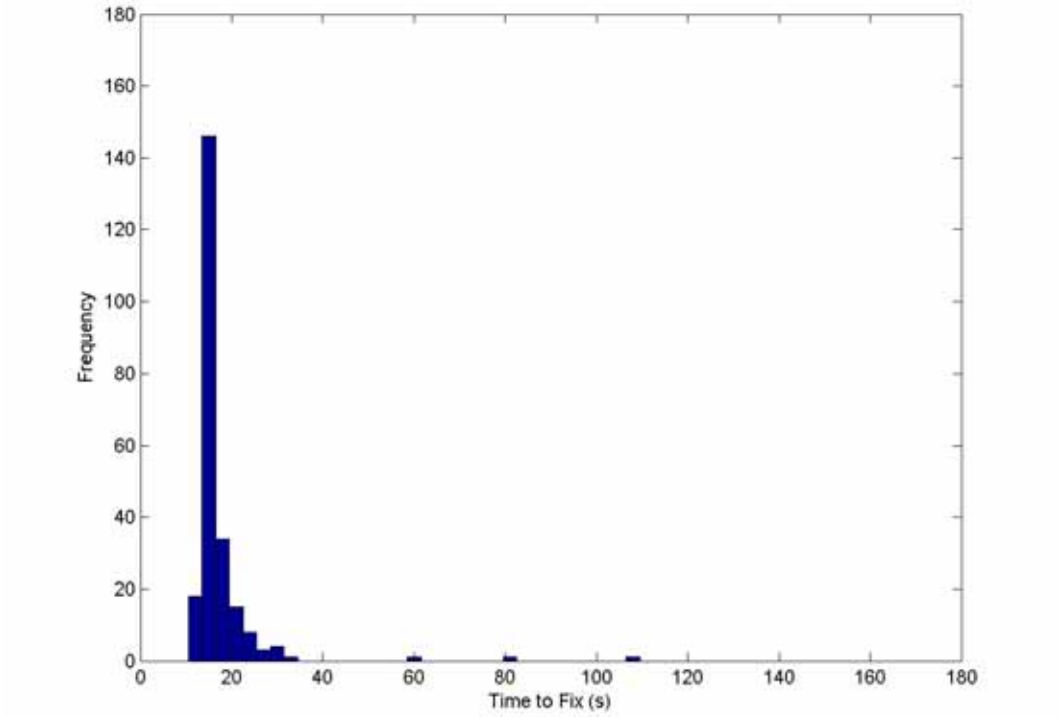

Figure 42 **Histogram over the time to fix with an ionospheric variability of 2.5 mm.**

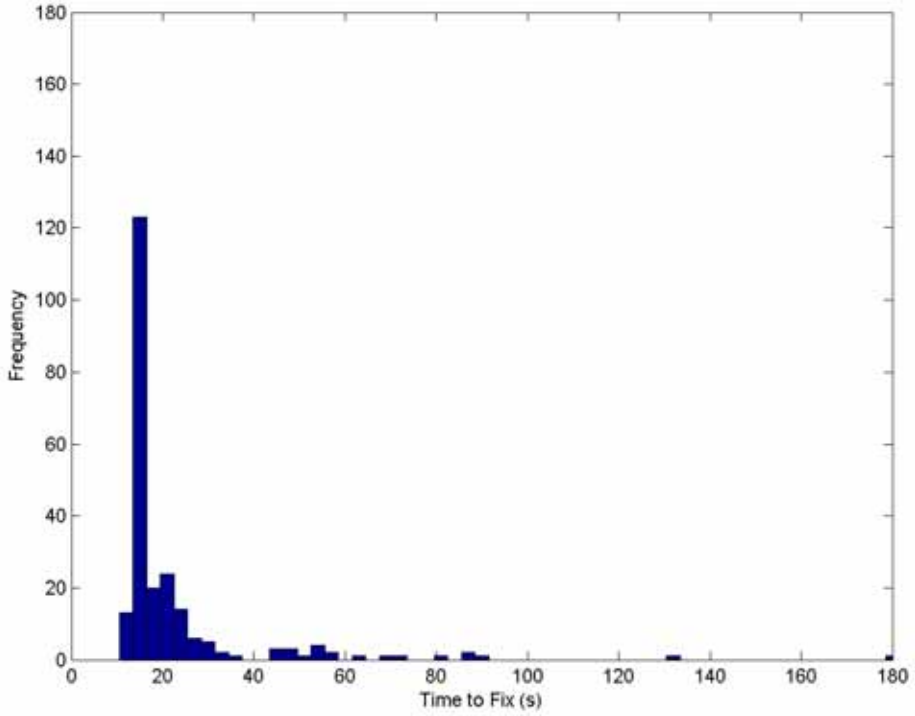

Figure 43 **Histogram over the time to fix with an ionospheric variability of 5 mm.**

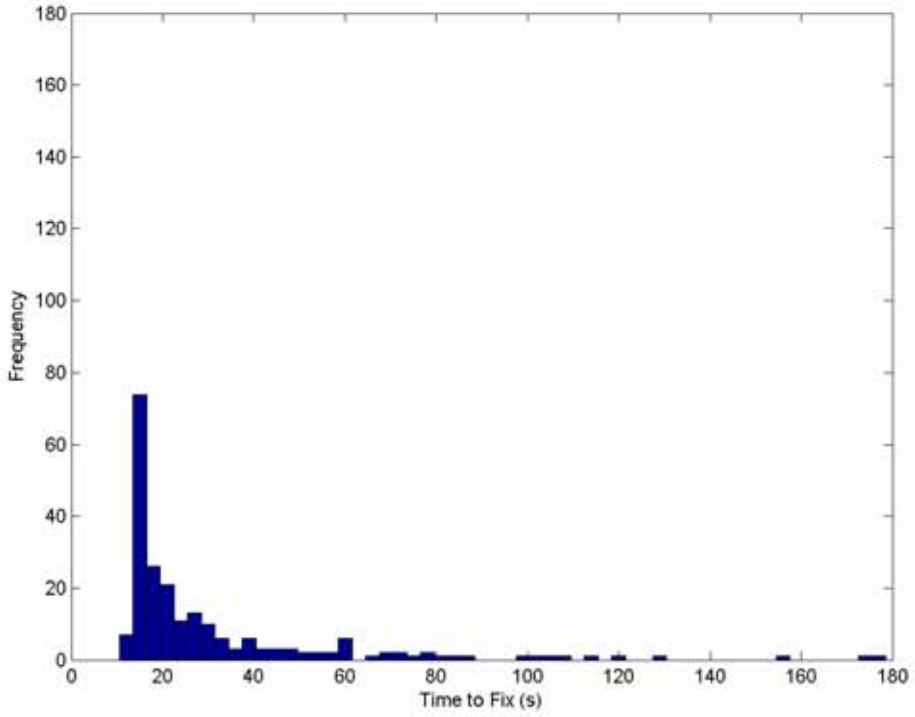

Figure 44 **Histogram over the time to fix with an ionospheric variability of 7.5 mm.**

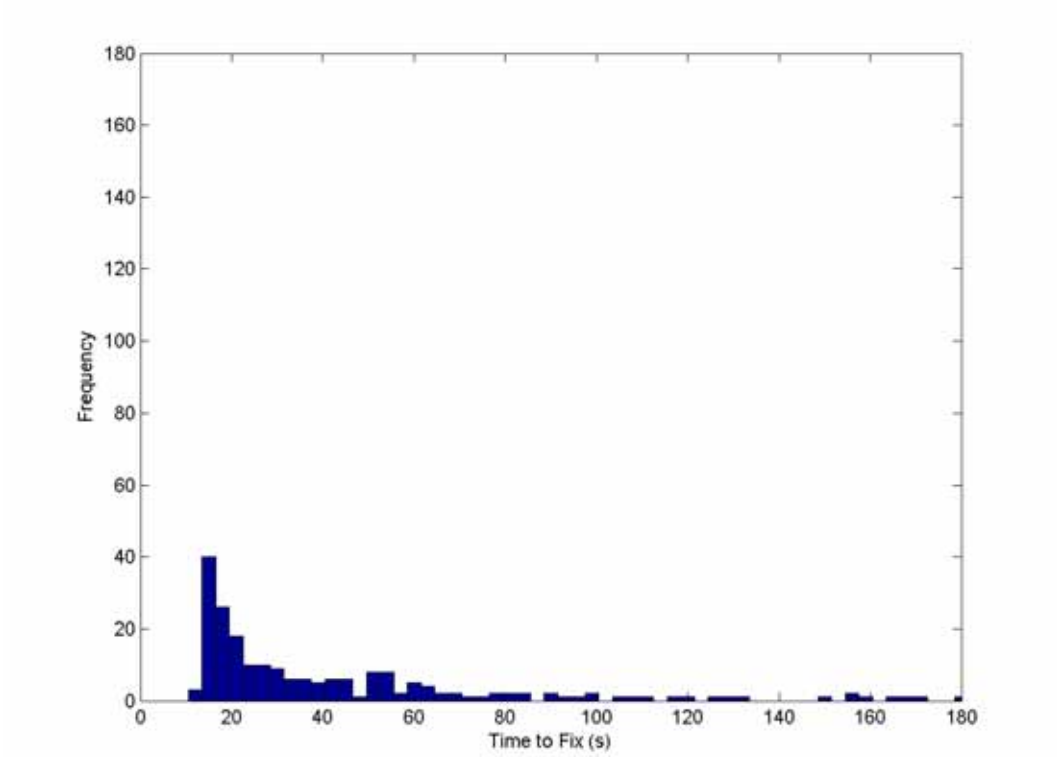

Figure 45 **Histogram over the time to fix with an ionospheric variability of 10 mm.**

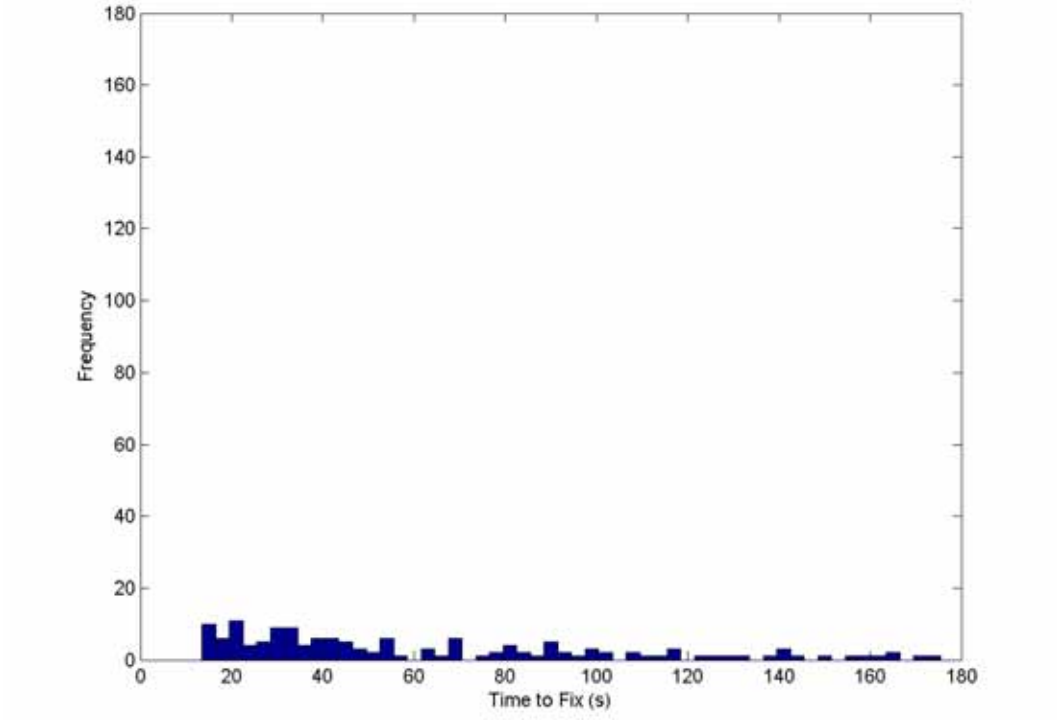

Figure 46 **Histogram over the time to fix with an ionospheric variability of 15 mm.**

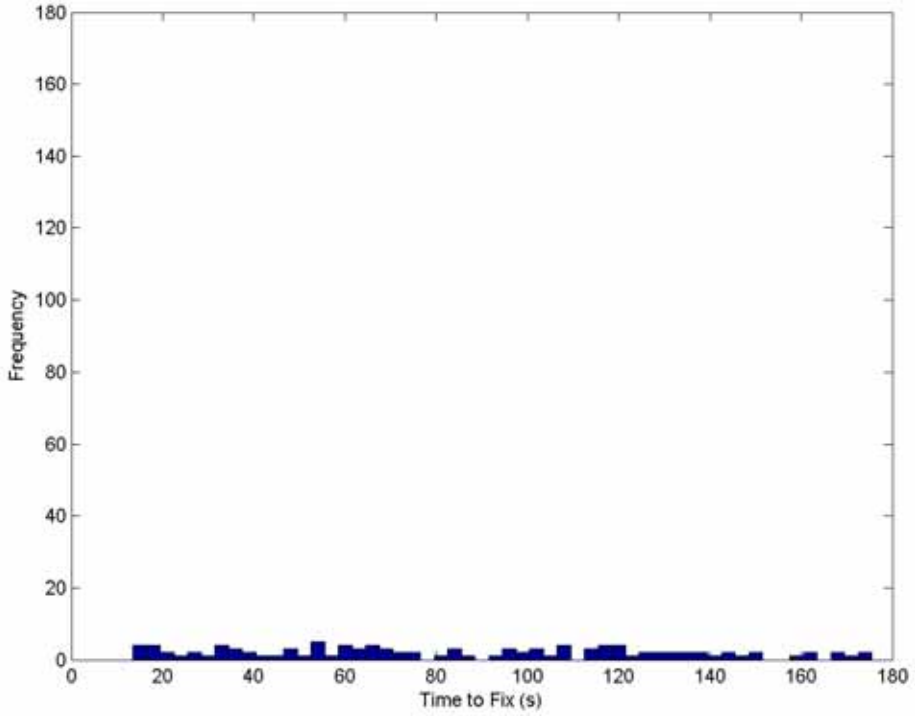

Figure 47 **Histogram over the time to fix with an ionospheric variability of 20 mm.**

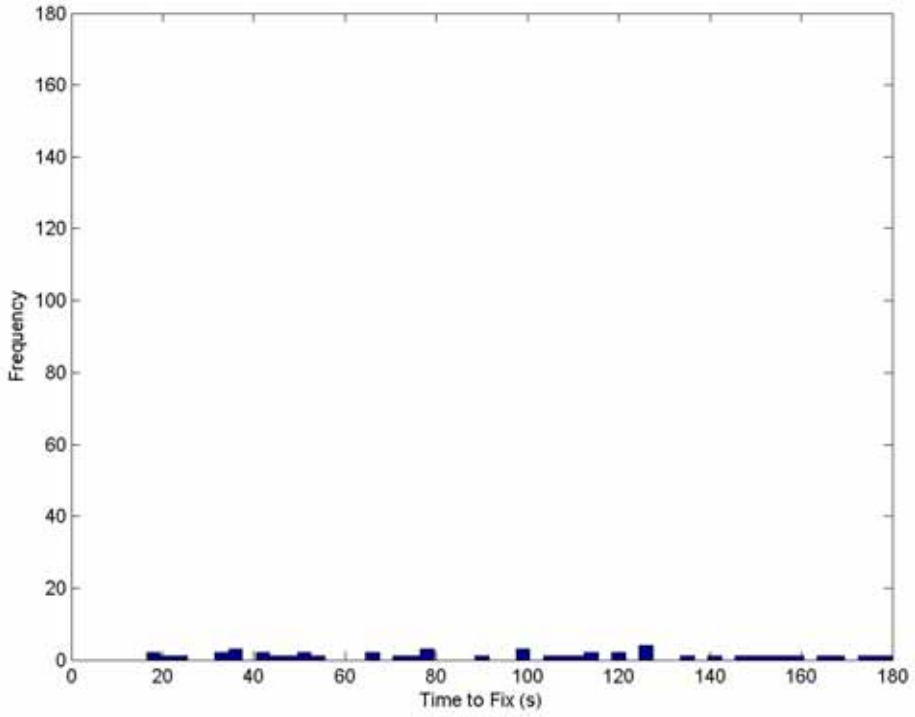

Figure 48 **Histogram over the time to fix with an ionospheric variability of 30 mm.**

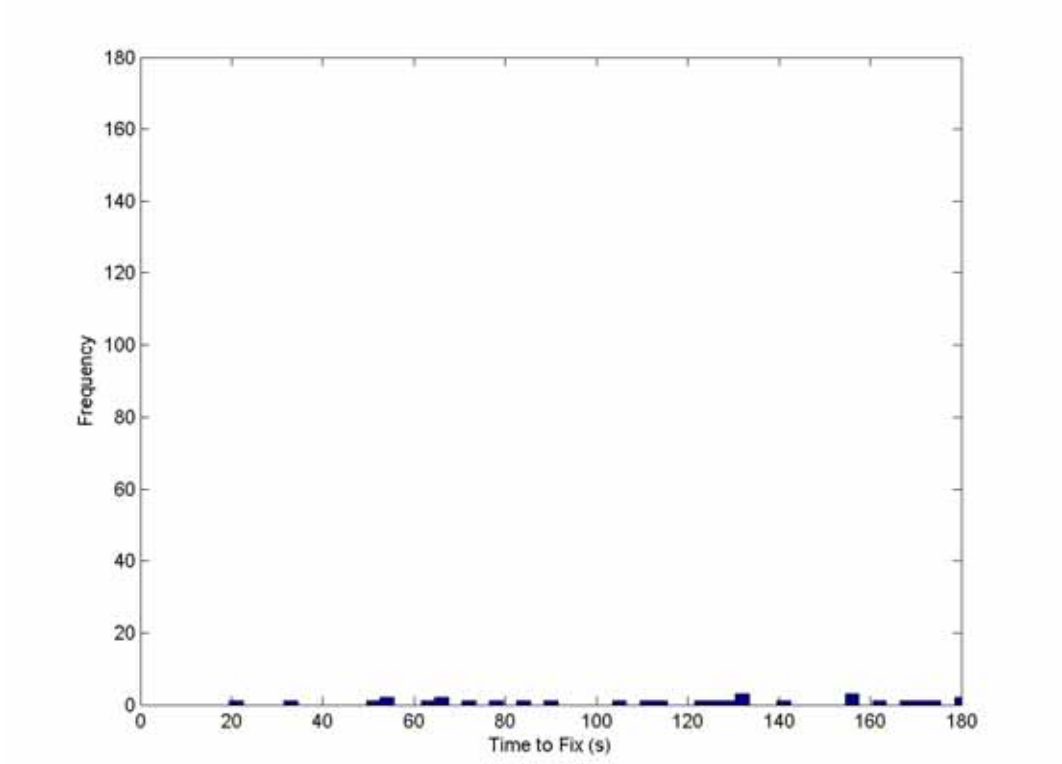

Figure 49 Histogram over the time to fix with an ionospheric variability of 40 mm.

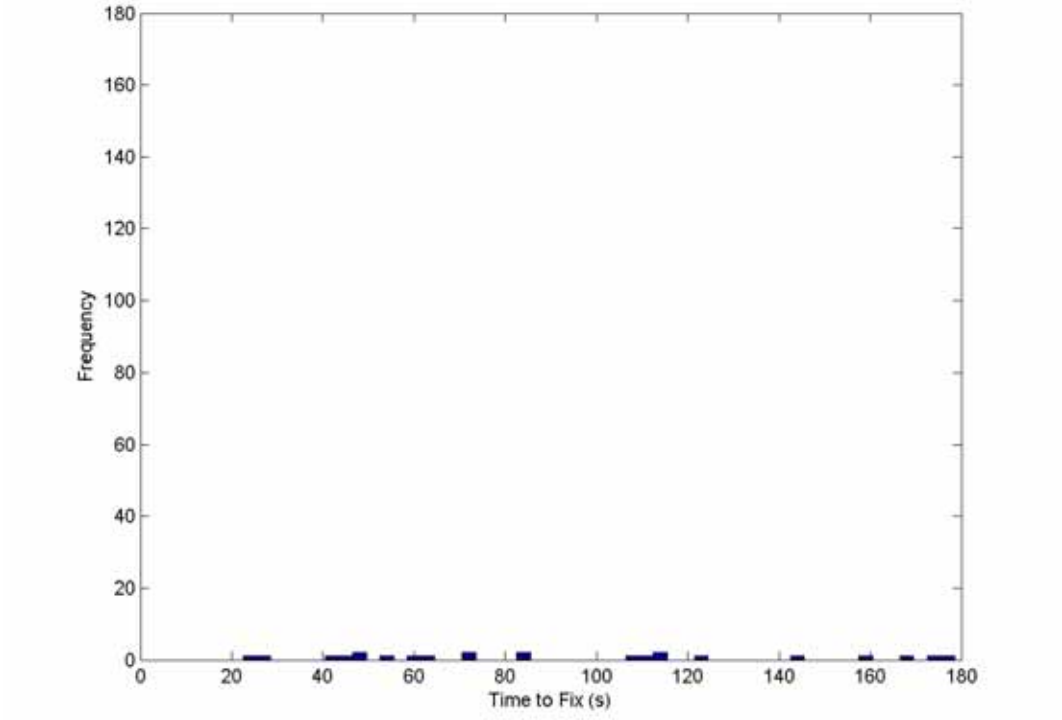

Figure 50 Histogram over the time to fix with an ionospheric variability of 50 mm.

By studying the time it takes for the rover to find a fix solution, we can see how it varies with the ionospheric variability. Figure 51 shows the relative number of occasions the rover finds the correct fix solution given different levels of ionospheric activity. When the rms error of the ionospheric delay errors below 10 mm, the rover is able to fix the

ambiguities more than 90% of the time. This ability decreases with increasing ionospheric variability and when the rms delay error is larger than 25 mm, the rover ability to fix is less than 50%.

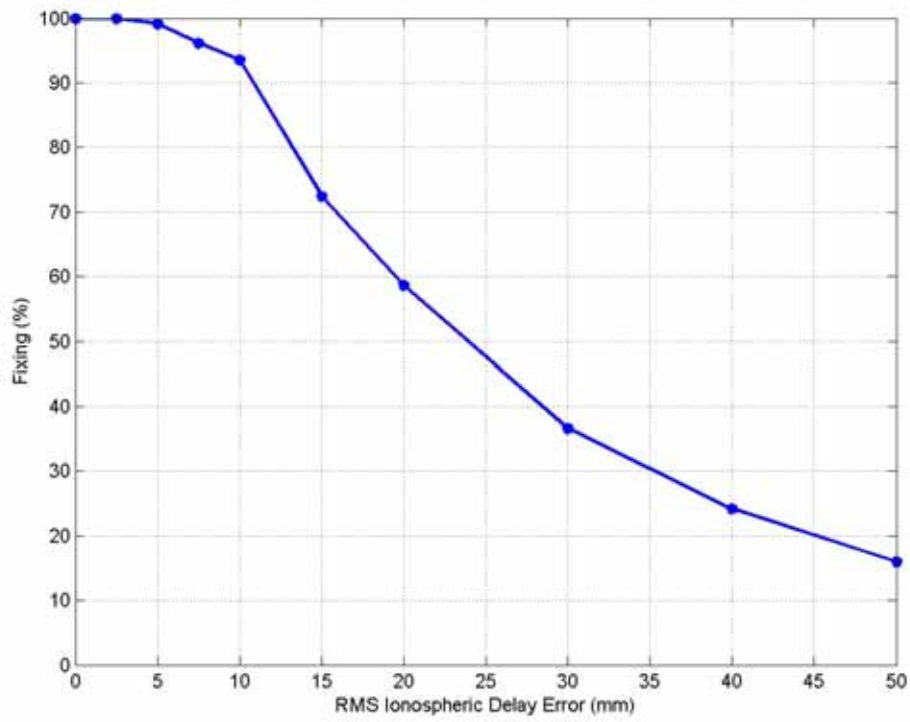

Figure 51 Fixing percentage as a function of the rms ionospheric delay error.

Figure 52 shows the rover mean time to fix as a function of the rms ionospheric delay error. For low ionospheric variability the rover is able to relatively quickly find a fix solution. However, already for a variability of 10 mm, the time to fix is more than 50 seconds and this time increases relatively linear with the ionospheric variability. For ionospheric delay errors above say 40 mm, the results are relatively uncertain due to the small number of fix solutions and consequently limited statistics.

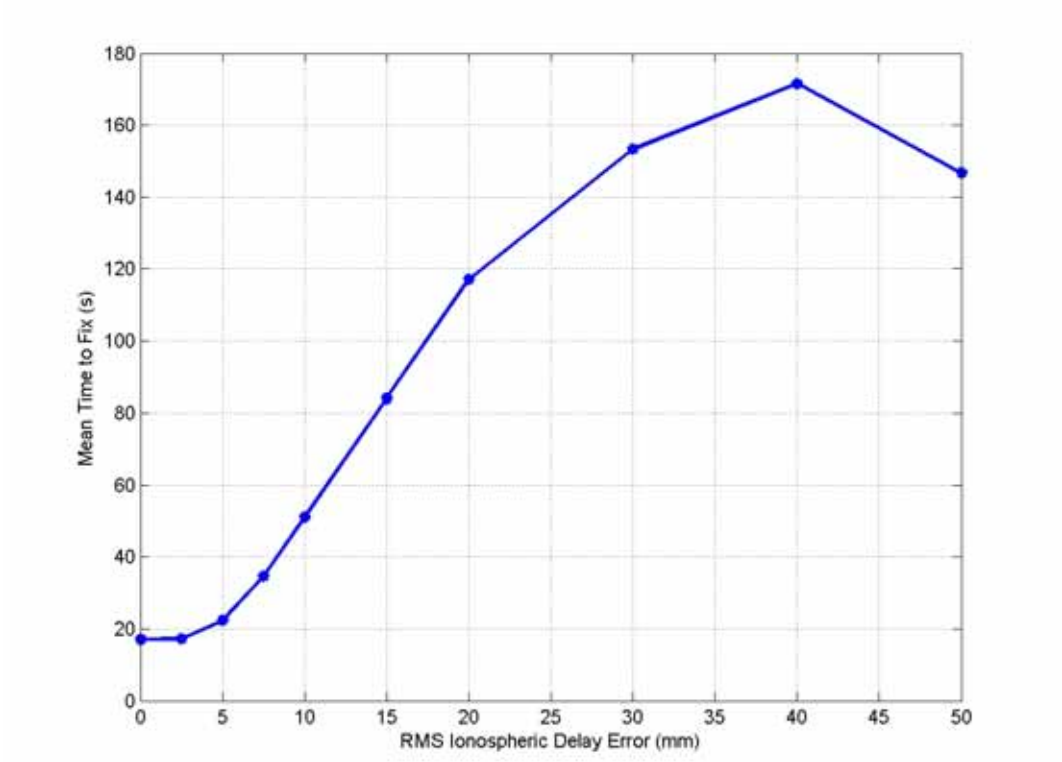

Figure 52 Mean time to fix as a function of the rms ionospheric delay error.

Based on the statistics for the ionospheric variability, shown in the previous section and the results presented above on the rovers ability to find fix solutions as a function of ionospheric variability, we can predict the rovers ability to fix solutions over the next solar maximum. Figure 53 shows the fixing percentage as a function of percentage of time. Here the different curves illustrate the results for the different geographical regions that we have studied. The figure illustrates the accumulated fixing percentage, that is it should be interpreted as for example for the southern most triangle 90% of the time, we have an ionospheric variability such that the rover has 70% chance of fixing the ambiguities correctly. Studying the combined results for the three geographical areas, we can say that approximately, 80% of the time, we have conditions such that a rover has at least 75% chance of fixing the solutions.

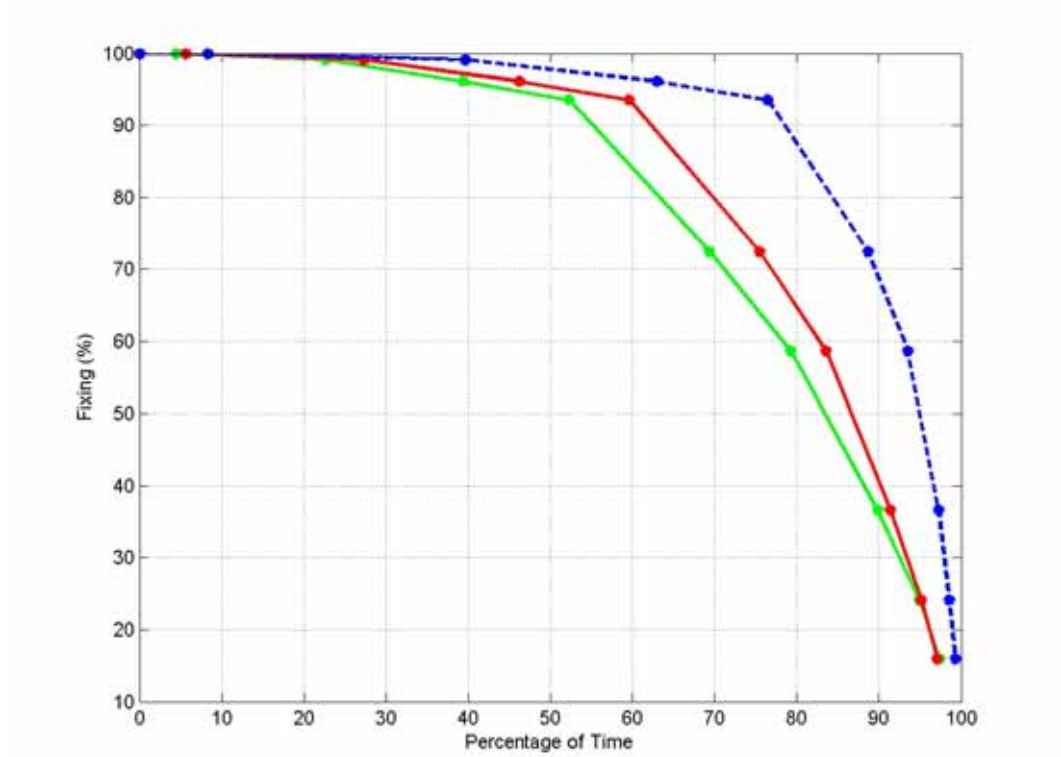

Figure 53 **Accumulated fixing percentage versus time coverage. Results from North Triangle are shown in green (solid line), Mid Triangle results are shown in red (solid line) and results from South Triangle in blue (dashed).**

Using the same methodology for the rover's time to fix, we can predict what it may look like during the next solar maximum. Figure 54 shows the rover's mean time to fix as a function of percentage of time. Also this figure shows the accumulated results. That is the figure should be interpreted as for the southern most triangle, the mean time to fix is less than 60 seconds 80% of the time.

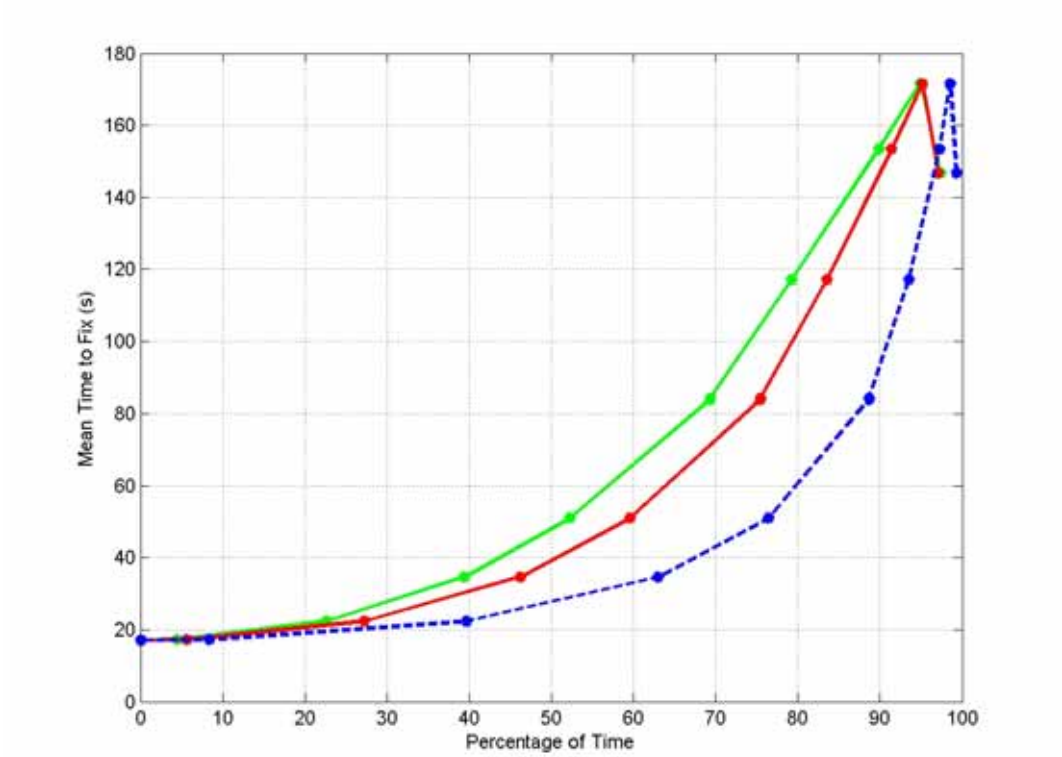

Figure 54 **Mean time to fix as a function of percentage of time. Results from North Triangle are shown in green (solid line), Mid Triangle results are shown in red (solid line) and results from South Triangle in blue (dashed).**

We also used RTCM v3 (896 cycles compared to 232 for RTCM 2.3). RTCM v3 has the potential to handle ionospheric variability better than v2.3. In v3 there is a message where statistical information on the expected ionospheric variability can be provided to the rover. We used that message in the simulation. The results from the RTCM v3 simulations are, however, similar to those where RTCM v2.3 are used. The general statistical information in v3 might be hard to utilize in a specific case. It could also happen that the equipment used in the simulations was not fully updated to handle the extra information.

3.3 Quality degradation

The ionospheric interpolation error described in the previous section will affect the vertical and horizontal position estimates since the differenced phase errors will map into different position errors primarily depending on their elevation dependence. In order to determine how much contributes to the position errors we follow the approach in *Emardson et al.*, [2009] and use the model

$$z + \partial z = H\left(x + \partial x\right) \tag{13}$$

Here the vector z contains the measurements, The vector δz contains the interpolation or measurement errors. In this report, we have used L1 only for the basic scenario. The vector x contains the parameters we want to estimate. These are three dimensional rover

position e_E, e_N, e_V, and a receiver clock offset l_o. δx contains the errors in the estimated parameters corresponding to the δz. The matrix H contains the partial derivatives matching the estimates with the measurement errors. The values in H depend primarily on the satellite constellation used. In this study, we have used a satellite constellation based on GPS and GLONASS during two weeks, from GPS week 1491 and 1492. This is the time period from August 3, 2008 to August 16, 2008. We have processed the data with 1 minutes interval. We have used an elevation cutoff angle of 13^o and the observations are weighted with *w=sin(elevation)*. Using this weighting, we form W as a diagonal matrix with values w on the diagonal. Using the modelling as described above, we can calculate the covariance of the errors in the estimated parameters as:

$$Cov(\partial\hat{x}) = \left(H^T WH\right)^{-1} H^T W \cdot Cov(\partial z) \cdot W^T H\left(H^T WH\right) \qquad (14)$$

We calculated theoretical values on the horizontal and vertical position error based on the ionospheric variability in Table 2. Table 4 shows the vertical position error for different values on the ionospheric variability for the two triangles. We can see that the errors for the southern triangle are significantly smaller than those for the mid triangle.

Table 4 Vertical position errors for all triangles, North Triangle, Mid Triangle and South Triangle based on contribution from the ionosphere only. The results reflect the five year study period and show rms, median, upper 90%, upper 95%, and upper 99%.

	RMS	**50%**	**90%**	**95%**	**99%**
Error all (mm)	38.1	16.8	55.4	79.3	141.3
Error North (mm)	42.9	21.2	67.3	89.7	145.4
Error Mid (mm)	42.6	18.0	61.4	88.1	161.5
Error South (mm)	27.1	13.2	35.8	50.3	101.3

In order to give a perspective on the size of the errors presented above we specify them together with the other errors affecting network-RTK. Table 5 and Table 6 show the total vertical and horizontal errors given the median value of the ionosphere variability as specified above together with the values on the other error contributions as taken from *Emardson et al.* [2009].

Table 5 Errors of the vertical position component for the mid and south study triangle.

Error source		Vertical Error (mm)			
		All	North	Mid	South
Ionosphere		16.8	21.2	18.0	13.2
Troposphere		20.9	20.9	20.9	20.9
Local Effects	Rover	5.6	5.6	5.6	5.6
	Reference sites	1.4	1.4	1.4	1.4
Total (rms)		27.4	30.3	28.2	25.4

Table 6 Errors of the horizontal position component for the mid and south study triangle.

Error source		Horizontal Error (mm)			
		All	North	Mid	South
Ionosphere		10.8	13.7	11.7	8.6
Troposphere		3.9	3.9	3.9	3.9
Local Effects	Rover	3.5	3.5	3.5	3.5
	Reference sites	0.9	0.9	0.9	0.9
Total (rms)		12.1	14.7	12.8	10.1

The results shown above indicate relatively large errors in the estimated positions due to ionospheric variability. We should, however, be aware of that when the ionospheric variability is large, L1 only processing will not be used by most systems. By using different combinations of L1 and L2, a large part of the ionospheric contribution will be removed. We have used two different setups for the rover when studying the impact ionospheric variability. Setup number one is based on the rover using L1 only for processing. Setup number 2 is based on a combined L1 and L2 processing. These setups are both default setting in the receiver we used. Figure 55 shows the rms of the horizontal position errors as a function of ionospheric variability. We can note from the figure that the L1 processing results in smaller position errors for conditions with low ionospheric variability while the combined L1, L2 processing results in better results for conditions with high ionospheric variability. In the figure is also shown the theoretical horizontal error based on the error propagation. This result is representative for the L1 only processing and also matches the experimental results relatively well. Figure 56 shows the corresponding results for the vertical position errors. Also here we can see that the theoretical results are in agreement with the experimental results for the L1 setup.

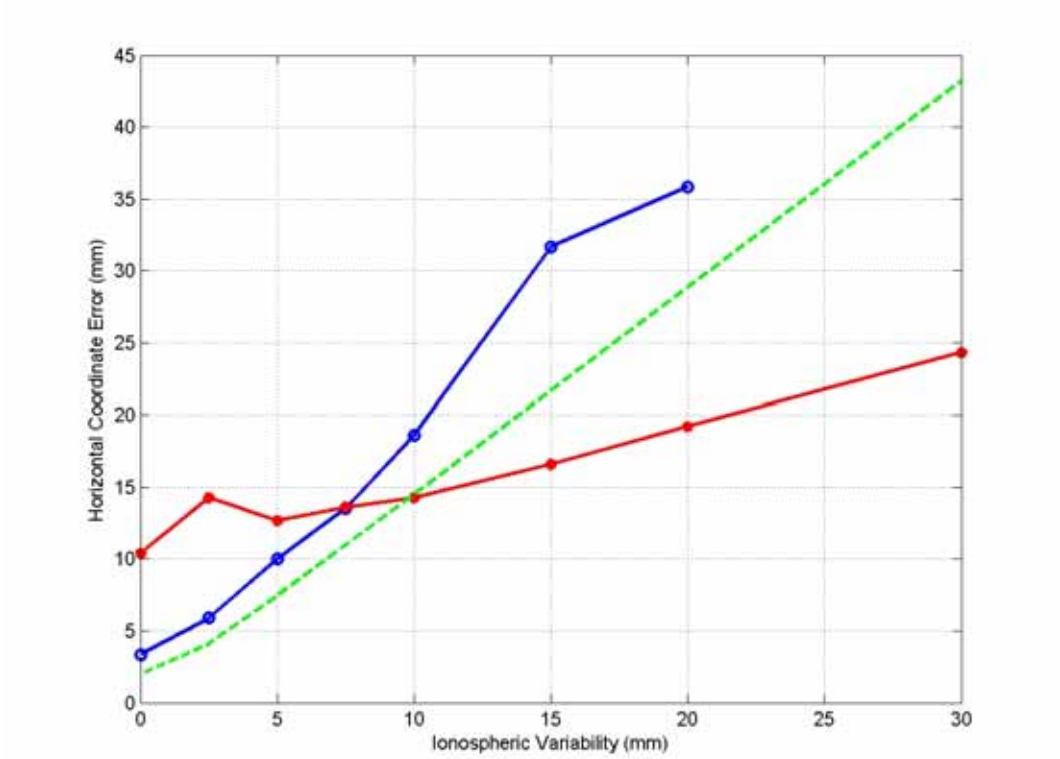

Figure 55 **Horizontal position errors as a function of ionospheric variability for the setup using L1 (blue), a combined L1 and L2 (red) and theoretical L1 model (green dashed).**

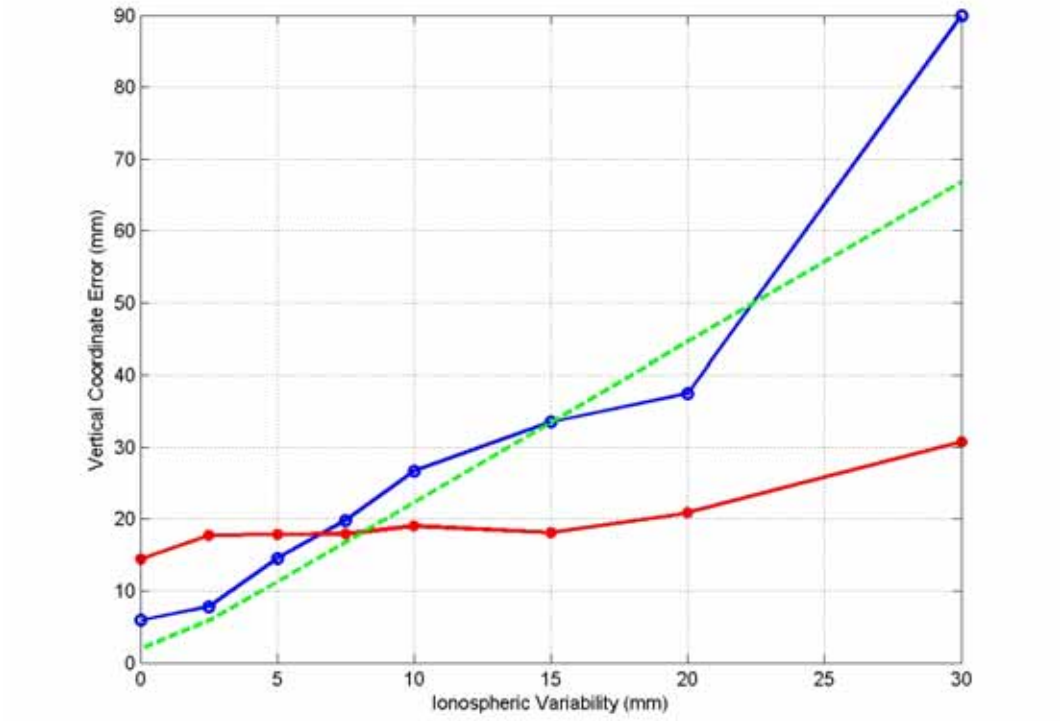

Figure 56 **Vertical position errors as a function of ionospheric variability for the setup using L1 (blue), a combined L1 and L2 (red) and theoretical L1 model (green dashed).**

Figure 57 shows the percentage of time that we can expect a specific vertical coordinate error using L1 only processing. In the figure is also shown the corresponding vertical coordinate error using L3 processing. Between 40% and 65% of the time ionospheric conditions are such that L1 processing performs better than L3 processing.

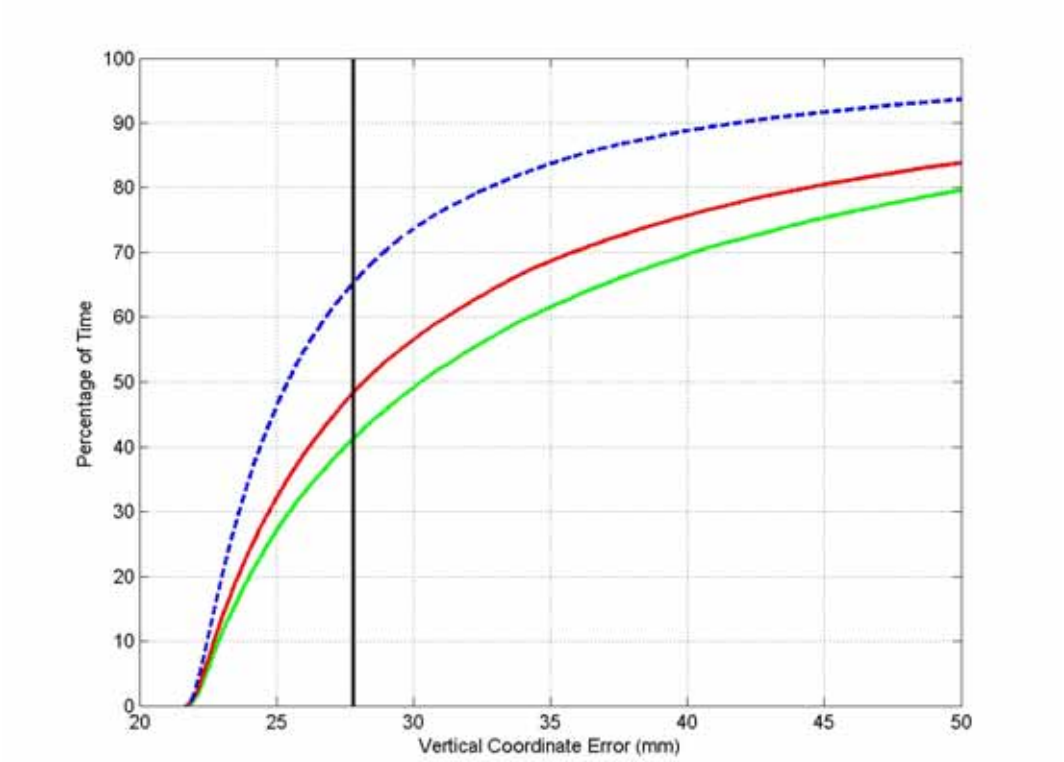

Figure 57 **Percentage of time with a specific vertical coordinate error using L1 only processing. The curves are for North Triangle (green), Mid Triangle (red), and South Triangle (blue dashed). The vertical bar indicates vertical coordinate error obtained using a L3 combination.**

4 Conclusion

The ionosphere will be a major issue for network-RTK in the coming years. Performance may be degraded both in terms of accuracy of the measurements and in terms of availability.

We find that the effect of the ionospheric spatial variability on network-RTK measurements is greater during night time than during day time. It is also clear that the effect is larger for northern Sweden than for the southern part. This is especially true during night time. The effect is also largest in the months October and November and smallest in June and July. Also the number of cycle slips is larger in northern Sweden than in southern Sweden. We find that when monitoring the ionosphere and its influence on network-RTK performance it is desirable to have several different geographical regions under observation. The effects in northern Sweden may, for example not be that relevant for a user in southern Sweden.

The effect due to temporal variations in the ionosphere causing scintillations seem to be a less serious problem for network-RTK users. Scintillations will presumably affect measurements that already are performed in difficult conditions in terms of, for example, satellite coverage.

With current equipment, we find that when conditions are such that the rms of the ionospheric delay errors is below 10 mm, which occurs some 70% of the time, a rover is able to fix the ambiguities more than 90% of the time. This ability decreases with increasing ionospheric variability and when the rms delay error is larger than 25 mm, which occurs some 10% of the time, the rover ability to fix is less than 50%. When measuring with network-RTK during the next solar maximum, approximately, 80% of the time, we have conditions such that a rover has at least 75% chance of fixing the solutions.

Overall the probability to find a correct fix solution when performing RTK measurements during the next solar maximum is approximately 85% and the mean time to fix is 55 seconds.

5 References

Alurkar, S.K., Solar and interplanetary disturbances, World Scientific Pub Co Inc., 1997.

Basu, S., Basu, S., Khan, K., Model of equatorial scintillations from in-situ measurements, Radio Sci., vol. 11, 821-832, 1976

Emardson, R., Jarlemark, P.O.J, Bergstrand S., Nilsson T., and Johansson J., Measurement Accuracy in Network-RTK, SP report 2009:23, ISBN 978-91-86319-10-6, 2009.

Emardson, R., Jarlemark, P.O.J, Bergstrand S., Johansson J., M. Lidberg, B. Jonsson, Measurement accuracy in network-RTK, Accepted for publication in BGG, 2010.

Gombosi , T.I., Physics of the Space Environment, Cambridge Atmospheric and Space Science Series, University of Michigan, Ann Arbor, ISBN-13: 9780521607681 | ISBN-10: 052160768X, DOI: 10.2277/052160768X.

Hargreaves, J.K., Thomas, L. and Davey, M.K., The solar-terrestrial environment: an introduction to geospace-the science of the terrestrial upper atmosphere, ionosphere, and magnetosphere, Cambridge University Press Cambridge, 1992.

Hoffman-Wellenhof B., H. Lichtenegger, and J. Collins, GPS: Theory and practice, *Springer Verlag, New York*, 1994.

Jokipii, J. R, Turbulence and Scintillations in the Interplanetary Plasma Annual Review of Astronomy and Astrophysics, vol. 11, p.1-28 DOI: 10.1146/annurev.aa.11.090173.000245, 1973.

Kedar S., Hajj, G. A., Wilson B. D., and Heflin M. B., The effects of the second order GPS ionospheric correction on receiver positions, Geophys. res. lett., doi:10.1029/2003GL017639, 2003.

Kelley, M.C., The Earth's Ionosphere: Plasma Physics and Electrodynamics, Academic Pr., 2009.

Kinter, P., Humphreys , T., Hinks , J., GNSS and Ionospheric Scintillation How to Survive the Next Solar Maximum, Inside GNSS, 2009.

Kivelson, M.G., and Russell, C. T., *Introduction to Space Physics*, red. M. G. Kivelson och C. T. Russell, Cambridge University Press, 1995.

Richmond, A. D., Thermospheric Dynamics and Electrodynamics SOLAR-TERRESTRIAL PHYSICS: BOSTON COLLEGE: 82AUG P.523, 1983.

Umeki, R., Liu, C.H., Yeh, K.C., Multifrequency spectra of ionospheric amplitude scintillations, J. Geophys. Res., vol. 82, 2752-2760, 1977.

Yeh, K. C., and Liu, C.H., Radio wave scintillations in the ionosphere, proc. IEEE, 70, 4, 324-360,1982.

http://ion.le.ac.uk/ionosphere/profile.html

http://en.wikipedia.org/wiki/Ionosphere

http://www.nwra.com/spawx/f10.html

http://www.ngdc.noaa.gov/stp/SOLAR/FLUX/flux.html

http://www.ngdc.noaa.gov/stp/SOLAR/ftpsolarradio.html#noonflux

http://en.wikipedia.org/wiki/Interplanetary_scintillation

http://www.ngdc.noaa.gov/stp/SOLAR/ftpsolarradio.html#noonflux

http://sidc.oma.be/sunspot-data/

http://www.swpc.noaa.gov/NOAAscales/index.html

Appendix I

In order to characterize the variability of the ionosphere on the spatial scales relevant for network-RTK, we used GPS data from the SWEPOS network. By forming the L4 combination of the signals received at the two GPS frequencies L1 and L2, we obtain a rough estimate of the signal variation in the ionosphere. This estimate, however, contains also potential non-ionospheric variations To correct for these effects, we used a method of subtraction of a L4 mean value without ambiguity fixing.

To perform this, we only used cycle slip free satellite passes where there were more than 1 hour long continuous tracking of the satellite signal and the observed elevation angle was above 20 degrees during this passage. The duration of such tracks was typically a couple of hours. From these satellite passages we form the L4 combination. This derived L4-combination contains potential non-ionospheric variations from multipath or local effects, receiver L1-L2 bias, satellite L1-L2 bias, and phase ambiguities. We remove the statistical contribution from multipath by using rms value of 3.8mm, from the multipath model developed in Close1[*Emardson et al*., 2009] and a typical elevation distribution from *Jarlemark et al.* [2010]. This value is subtracted from the L4-statistics.The receiver L1-L2 bias variation is considered to be relatively small at constant receiver temperatures [*Rieck et al*., 2003]. The satellite L1-L2 biases are in general considered to be constant over several hours. The constant phase ambiguity offsets does not contribute to the variations. Hence, we conclude that the remaining part is due mainly to ionospheric variations.

In order to assess the method described above and verify that we are not missing any ionospheric variations by the removal of the bias by averaging, we made correlation plots of mapped data from 20 hours with values according to the percentiles 50, 95 99 from each "triangle"Figure 58, Figure 59, and Figure 60 show the corresponding correlation plots. We can see that the de-correlation times are typically around 15 minutes. We used satellite passes longer than 1 hour. If significant variability were of time scales around 1 hour, that would have been visible in the correlation plots. Hence, we conclude that no significant ionospheric variability have been removed using our technique.

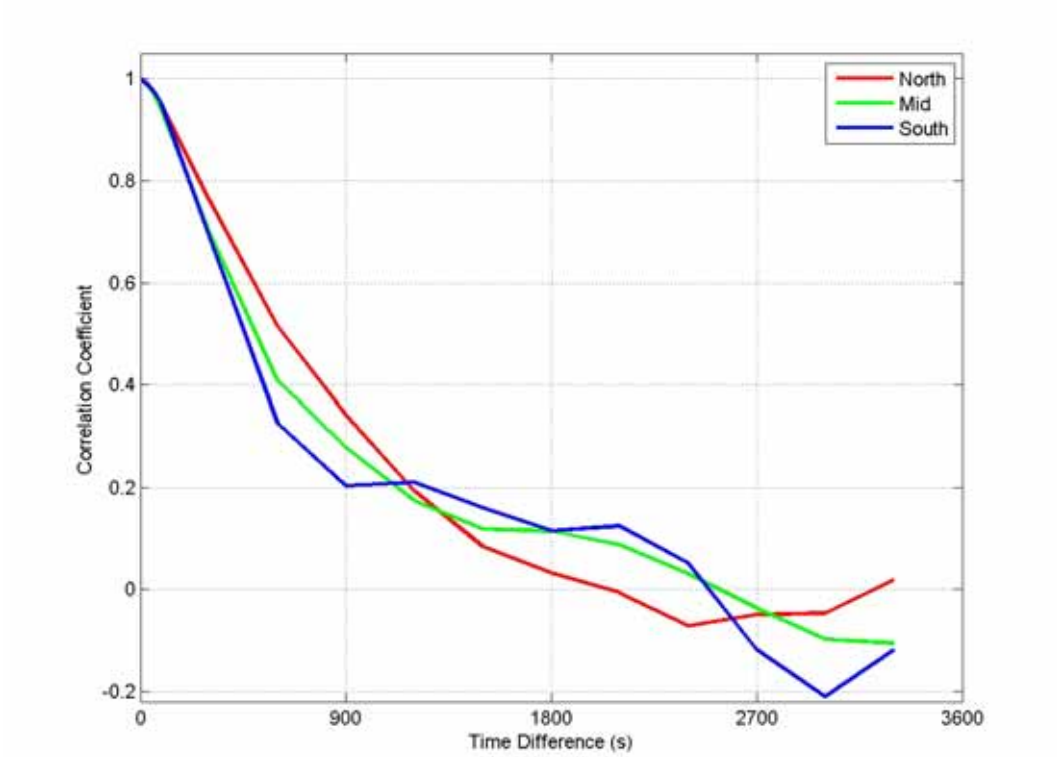

Figure 58 **Correlation for the 50 percentile for the North, Mid, and South triangle.**

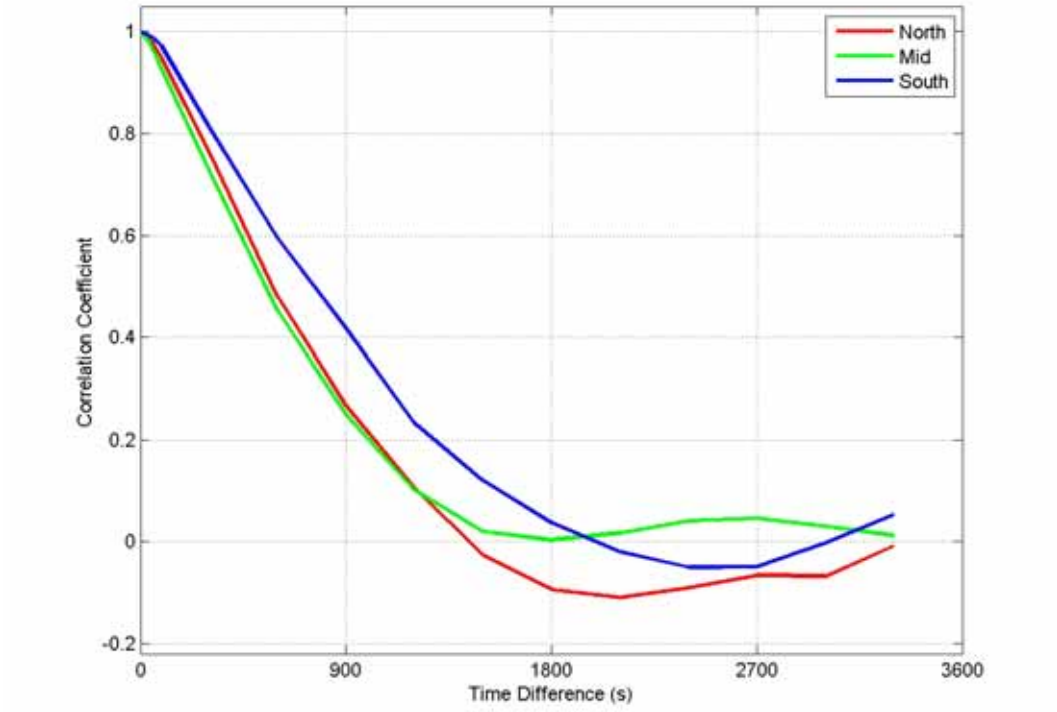

Figure 59 **Correlation for the 95 percentile for the North, Mid, and South triangle.**

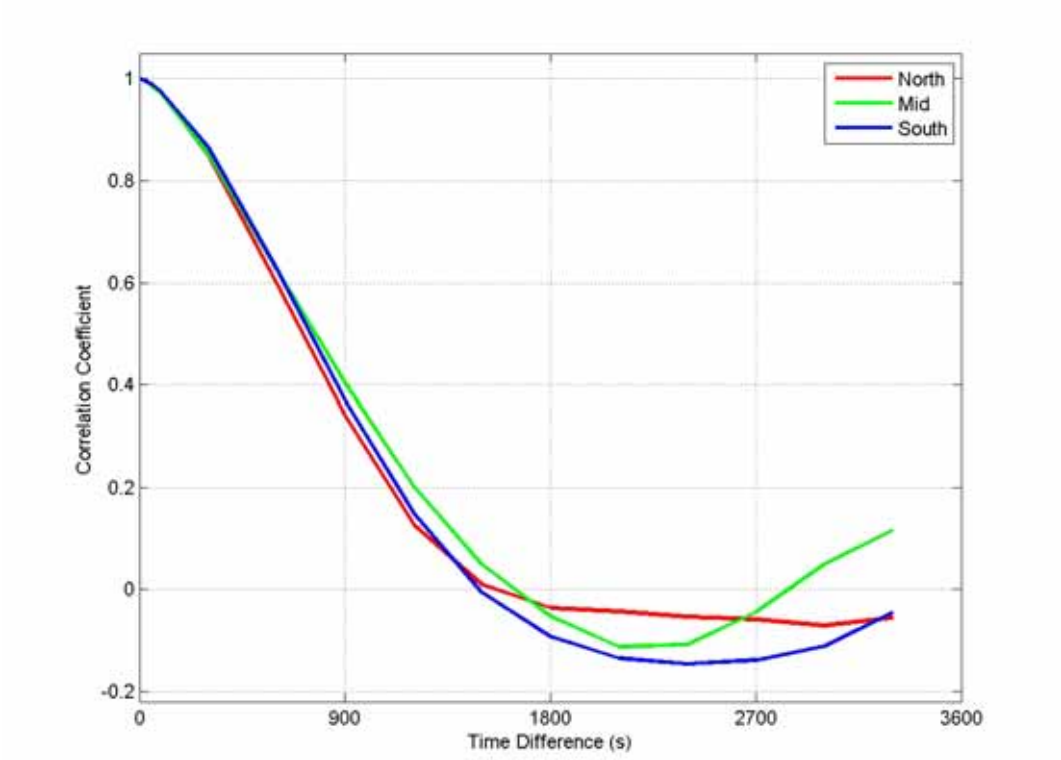

Figure 60 Correlation for the 99 percentile for the North, Mid, and South triangle.

The de-correlation times of 15 minutes are approximately also what could be expected from a static spatial feature following the sun. It typically passes a distance of 250 km (characteristic size for the triangles used for this study) at latitude 60^{o} in 1000 s.

In this report we use the ionospheric variability from the L4 estimate to predict the effects on L1. There we assume a quadratic dependence of the ionospheric effect with signal frequency. However, signal delay terms of higher order exist. The dominant part is a third order effect originating from the earth magnetic field. [*Kedar et al*., 2003] This effect is relatively small and the magnetic field can be considered constant over the spatial scales relevant for network-RTK. Hence, the size of this effect is negligible in this study.

References

Emardson, R., Jarlemark, P.O.J, Bergstrand S., Nilsson T., and Johansson J., Measurement Accuracy in Network-RTK, SP report 2009:23, ISBN 978-91-86319-10-6, 2009.

Jarlemark, P.; Emardson, R.; Johansson, J.; Elgered, G., Ground-Based GPS for Validation of Climate Models: The Impact of Satellite Antenna Phase Center Variations , *Geoscience and Remote Sensing, IEEE Transactions on* , vol 48, 10,3847-3854, doi: 10.1109/TGRS.2010.2049114, 2010.

Kedar S., Hajj, G. A., Wilson B. D., and Heflin M. B., The effects of the second order GPS ionospheric correction on receiver positions, Geophys. res. lett., doi:10.1029/2003GL017639, 2003.

Rieck, C., Jarlemark, P.O.J, Jaldehag, K., and Johansson, J., Thermal Influence on the Receiver Chain of GPS Carrier Phase Equipment for Time and Frequency Transfer, Proc. 2003 IEEE International Frequency Control Symposium, 2003.

Appendix II

We aim at characterizing the full sky ionospheric variability with one representative value. In order to find such a representative value, we scale the observations with respect to their elevation angle using a "thin shell mapping" (eq 5). As a result, the one value is then a mean "zenith" value of the ionospheric variability. Figure 61, Figure 62, and Figure 63 show the calculated ionospheric variability as a function of elevation angle for scaled and unscaled observations for periods of low, mid, and high ionospheric activity respectively. The scaling follows the natural elevation scaling for the low to mid(50%) variabilities. For the periods with a high variability, the unscaled values are relatively flat, i.e., independent of the elevation angle. Using the scaling of such observations will result in low elevation contributions far too small, maybe with exceptions for the southern triangle. Hence, during high ionospheric variability an unscaled average may be a better representation of the ionospheric conditions.

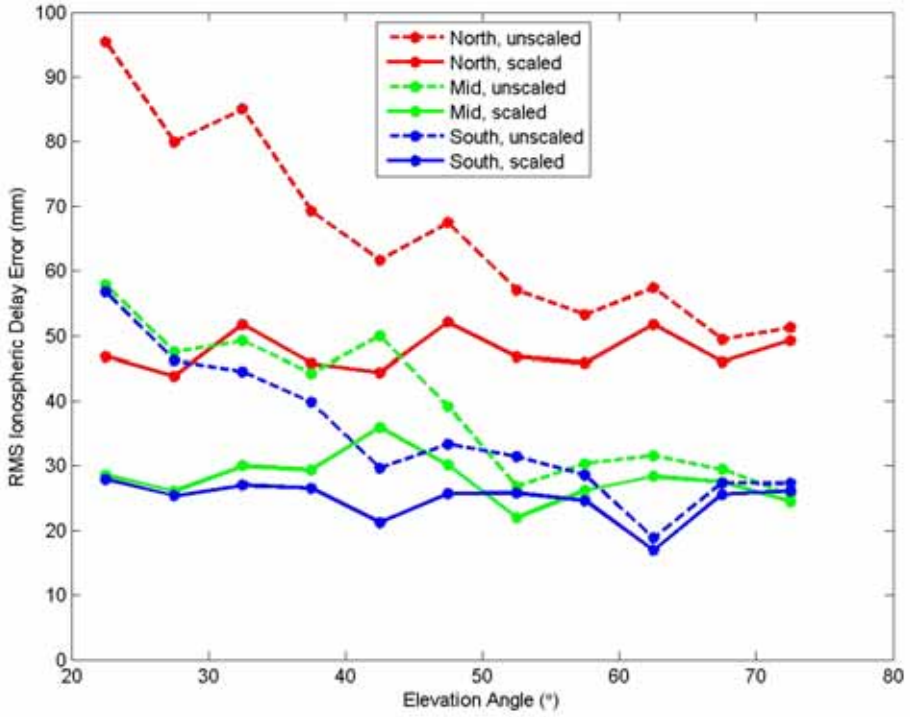

Figure 61 **Ionospheric variability as a function of elevation angle for scaled and unscaled observations for periods of low ionospheric activity.**

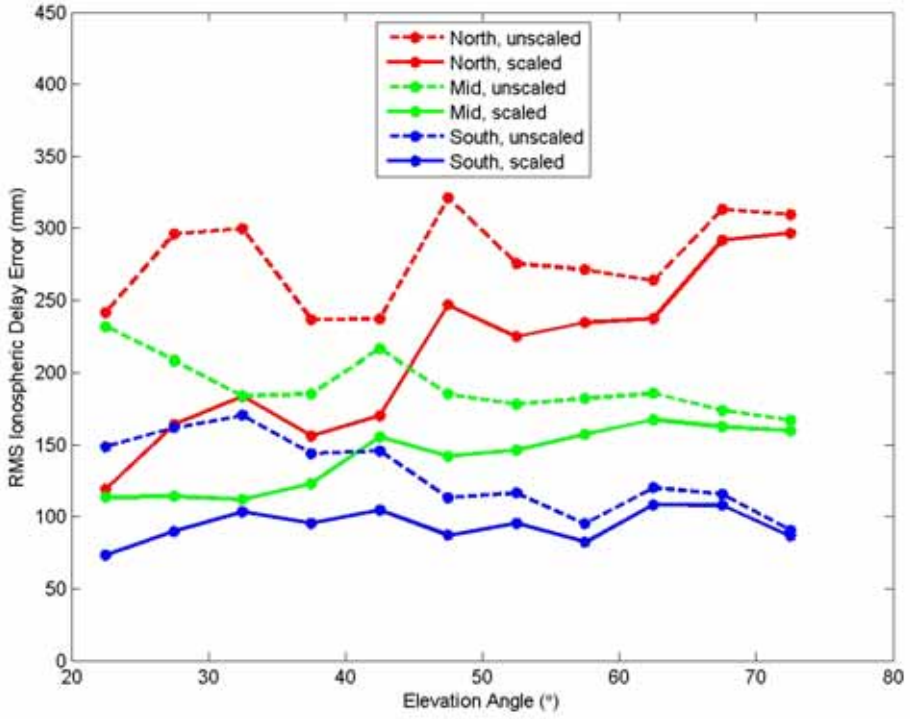

Figure 62 **Ionospheric variability as a function of elevation angle for scaled and unscaled observations for periods of mid ionospheric activity.**

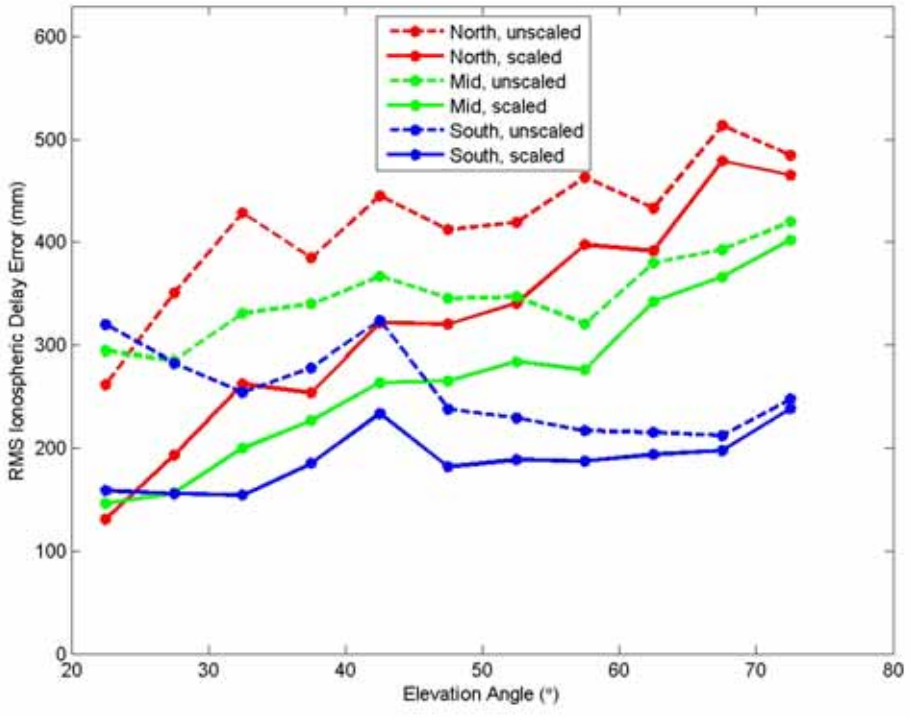

Figure 63 **Ionospheric variability as a function of elevation angle for scaled and unscaled observations for periods of high ionospheric activity.**

Appendix III

The distances between the reference stations in the triangles we have used to calculate statistics for the ionospheric variability are larger than those we assume for a standard reference network, i.e., with 70 km between the reference sites. In order to use the results for such networks, we have scaled the results using a distance scale factor. This scaling is based on studies where we use different sizes of triangles for interpolation. Figure 64 shows the three triangles we use to find an relevant model for spatial scaling. The three triangles consisting of nearby, but no common stations. We use a model as:

$$\sigma^2 = \sigma_0^2 \cdot d^{\alpha}$$

Where σ^2 is the variance of the interpolation error, and α determines the scaling with the separation distance *d*

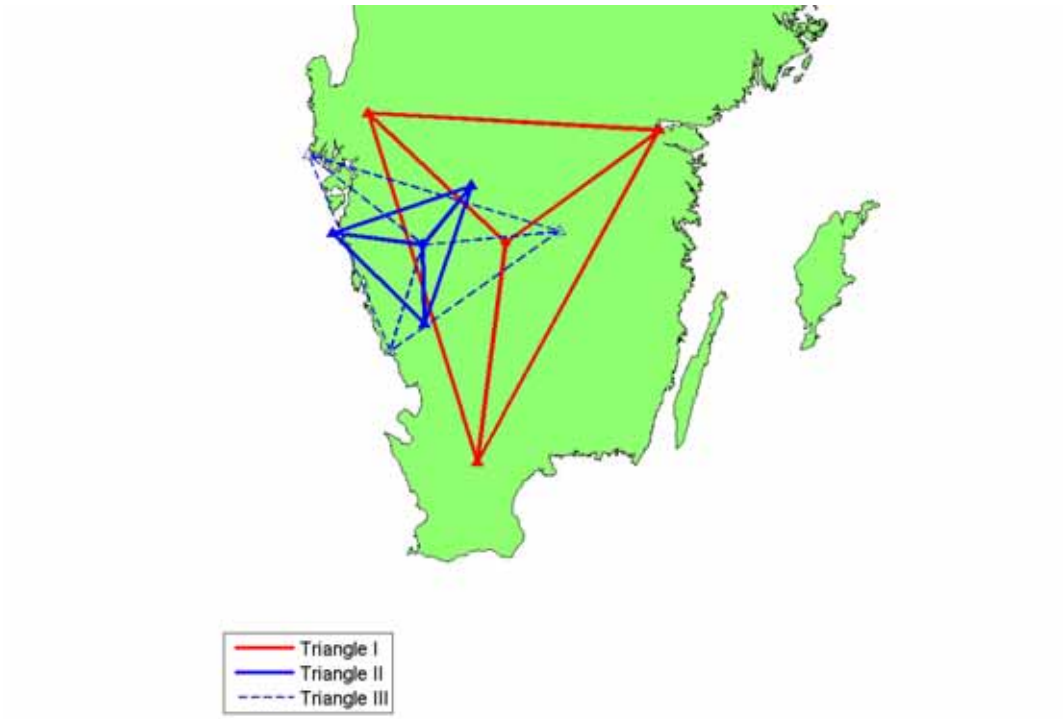

Figure 64 **The three triangles used to determine the spatial scaling of the ionospheric variability.**

Triangle I , which is identical to the "south" triangle in this report has a 290 km mean separation between the 3 reference stations. Triangle II has a 191 km mean separation between the reference stations. Triangle III has a 118 km mean separation between the reference stations.

Figure 65 shows the scaling between Triangle I and Triangle II. We have used data for slightly more than a year (from the fall 2002 and almost complete 2003) to study the relation between the interpolation errors for the triangles.A least squares fit to the data gives α equal to 2.29.

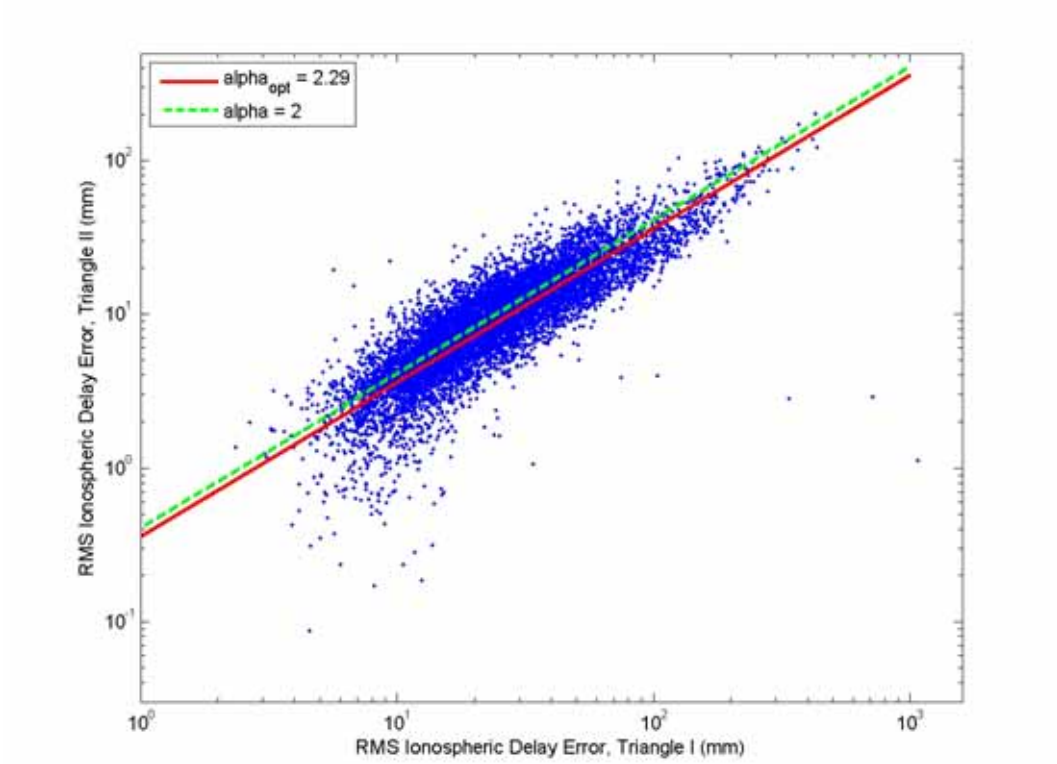

Figure 65 Scaling between Triangle I and Triangle II.

We made the same comparison for a period later, away from the solar max, using data from the main part of 2007. Here we compare triangle I with triangle II and triangle III The results are shown in Figure 66 and Figure 67. For these data sets, we find that the best fit to the data is for α approximately equal to 1.5.

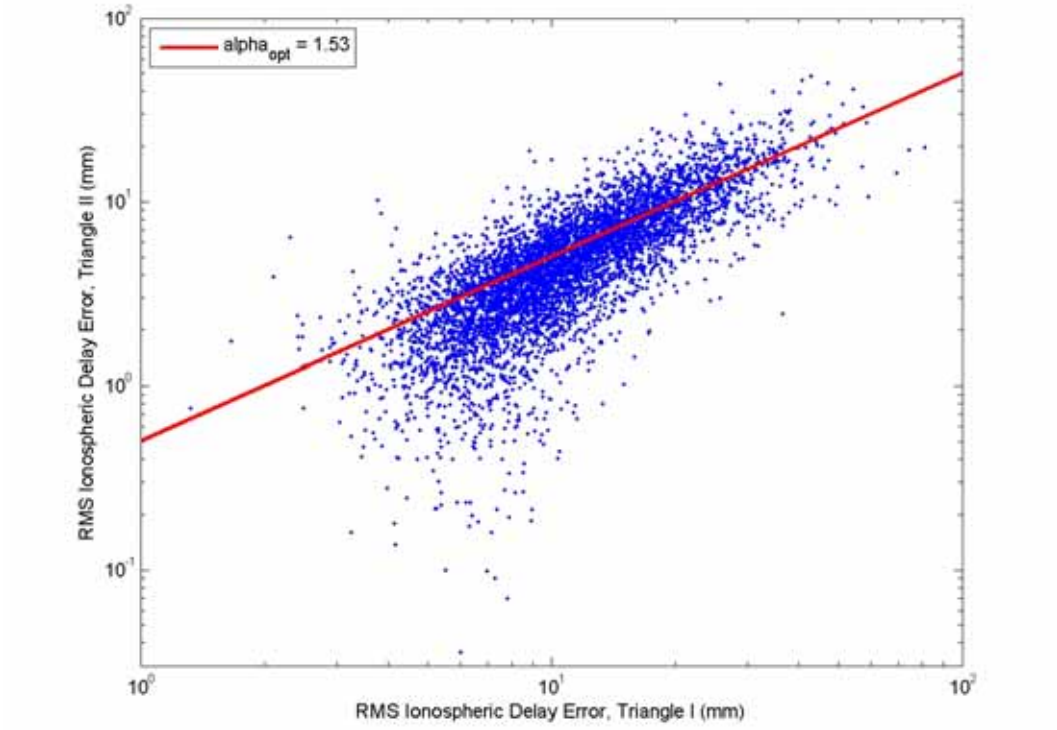

Figure 66 Scaling between Triangle I and Triangle II.

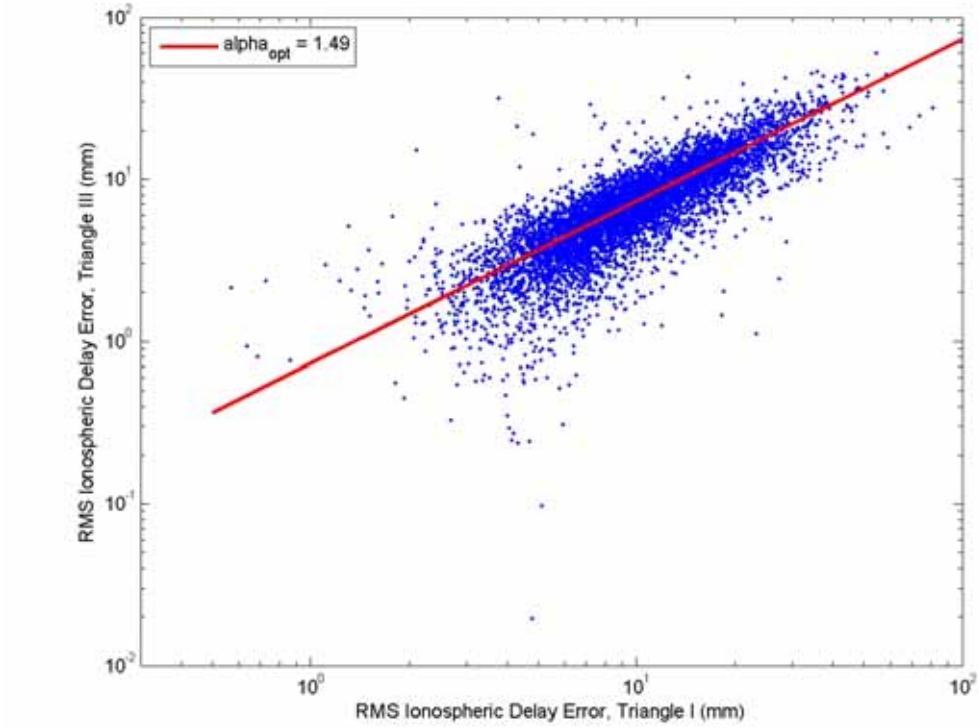

Figure 67 Scaling between Triangle I and Triangle III.

An optimal value for α may vary. Based on the comparisons above we use α=2 for the spatial scaling in this report.

Appendix IV

In the simulations presented in section 3.2, we assume that all satellite observations are affected by the ionospheric variability. If a single satellite observation contributes with almost all the variability, the rover may be able to discard such observations and thereby be less affected by the variability than shown by the simulations. In order to verify that the variability is distributed among more than one satellite observation, we studied 20 hours of data from the 50, 95, and 99 percentiles and the three different geographical regions. Figure 68 shows the relative change in ionospheric variability when omitting the satellite observation with the largest contribution.. The dashed curve shows an expected result if the satellite contributions follow a Gaussian distribution. We can see that the data relatively well agrees with what could be expected from a Gaussian distribution. If a single satellite observation would have contributed with the major part of the variability, the deviation from the Gaussian model would have been much larger.

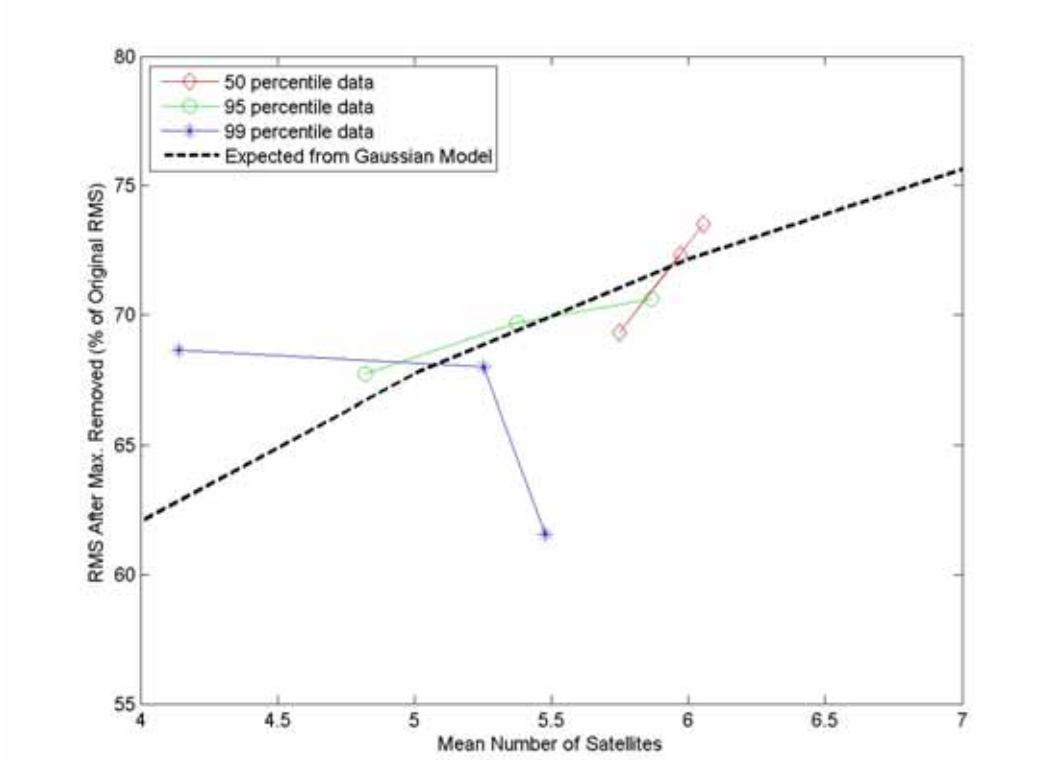

Figure 68 **Relative change in ionospheric variability when omitting the satellite observation with the largest contribution. This is shown for 50, 95, and the 99 percentile. The dashed curve shows an expected result if the satellite contributions follow a Gaussian distribution.**

SP Technical Research Institute of Sweden develops and transfers technology for improving competitiveness and quality in industry, and for safety, conservation of resources and good environment in society as a whole. With Sweden's widest and most sophisticated range of equipment and expertise for technical investigation, measurement, testing and certification, we perform research and development in close liaison with universities, institutes of technology and international partners.

SP is a EU-notified body and accredited test laboratory. Our headquarters are in Borås, in the west part of Sweden.

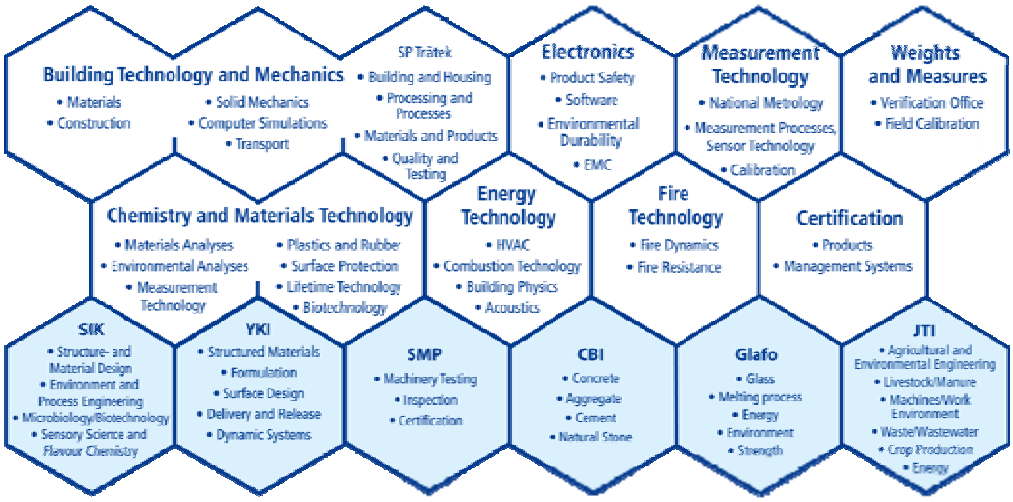

SP consists of eight technology units and six subsidiary companies. Three of the companies, CBI, Glafo and JTI are each 68 % owned by SP and 48 % by their respective industries.

SP Technical Research Institute of Sweden
Box 857, SE-501 15 BORÅS, SWEDEN
Telephone: +46 10 516 50 00, Telefax: +46 33 13 55 02
E-mail: info@sp.se, Internet: www.sp.se
www.sp.se

Measurement Technology
SP Report 2011:80
ISBN 978-91-87017-13-1
ISSN 0284-5172